Stratospheric Mountain Waves Trailing across Northern Europe

ANDREAS DÖRNBRACK[a]

[a] *Institute of Atmospheric Physics, DLR Oberpfaffenhofen, Weßling, Germany*

(Manuscript received 11 October 2020, in final form 2 May 2021)

ABSTRACT: Planetary waves disturbed the hitherto stable Arctic stratospheric polar vortex in the middle of January 2016 in such a way that unique tropospheric and stratospheric flow conditions for vertically and horizontally propagating mountain waves developed. Coexisting strong low-level westerly winds across almost all European mountain ranges plus the almost zonally aligned polar-front jet created these favorable conditions for deeply propagating gravity waves. Furthermore, the northward displacement of the polar night jet resulted in a widespread coverage of stratospheric mountain waves trailing across Northern Europe. This paper describes the particular meteorological setting by analyzing the tropospheric and stratospheric flows based on the ERA5 data. The potential of the flow for exciting internal gravity waves from nonorographic sources is evaluated across all altitudes by considering various indices to indicate flow imbalances as δ, Ro, Ro_{ξ}, $\mathrm{Ro}_{\perp}$, and ΔNBE. The analyzed gravity waves are described and characterized. The main finding of this case study is the exceptionally vast extension of the mountain waves trailing to high latitudes originating from the flow across the mountainous sources that are located at about 45°N. The magnitudes of the simulated stratospheric temperature perturbations attain values larger than 10 K and are comparable to values as documented by recent case studies of large-amplitude mountain waves over South America. The zonal means of the resolved and parameterized stratospheric wave drag during the mountain wave event peak at -4.5 and $-32.2\,\mathrm{m\,s^{-1}\,day^{-1}}$, respectively.

KEYWORDS: Atmosphere; Mountain waves; Stratosphere; Numerical weather prediction/forecasting; Reanalysis data

1. Introduction

The motivation to compile the following material is twofold. First, I present a meteorological analysis of the tropospheric and stratospheric flows crossing Central and Northern Europe for a period of time in mid-January 2016 that has attracted scientific interest and led to a couple of journal publications (Bramberger et al. 2018; Woiwode et al. 2018; Bossert et al. 2020). During this time period from 10 to 13 January 2016, strong gravity wave activity was diagnosed over Europe that stretched from the upper troposphere to the middle atmosphere.

In search for the sources of the gravity waves, for their atmospheric propagation conditions, I explored meteorological analyses. The deeper I sounded, the further down I probed and pressed, the more I found about the manifold processes occurring during this period. In analogy to the first sentence of Thomas Mann's *Joseph and His Brothers*, I could write, Very deep is the well of the facts. Should we not call it bottomless? And I continue citing and using only slight modifications of his wording: Indeed bottomless and no matter to what hazardous lengths we let out our lines of research they still withdraw again, and further, into the depths. Again and further are the right words, for the unresearchable plays, a kind of mocking game with our researching ardors; it offers apparent holds and goals, behind which, when we have gained them, new reaches still open out—as happens to the coastwise voyager, who finds no end to his journey, for behind each headland of clayey dune he conquers, fresh headlands and new distances lure him on.[1] Thus, the material I will present here might be considered as a temporary halt of a journey. I decided to present one, yet, rather plausible explanation of the numerical simulation results I analyzed in the process of searching. However, new knowledge and insights may arise if other tools and diagnostics are applied to analyze the selected time period.

The second motivation arises from the ability of the latest high-resolution analysis and reanalysis data to resolve gravity waves. Here, I mainly use the operational, high-resolution deterministic forecasts and analyses (HRES) of the Integrated Forecast System (IFS) as well as the most recent reanalysis data of the European Centre for Medium-Range Weather

Denotes content that is immediately available upon publication as open access.

Supplemental information related to this paper is available at the Journals Online website: https://doi.org/10.1175/JAS-D-20-0312.s1.

Corresponding author: Andreas Dörnbrack, andreas.doernbrack@dlr.de

[1] Cited and modified after Thomas Mann, "Prelude: Descent into Hell" from *Joseph and His Brothers*, translated by H. T. Lowe-Porter, New York, Alfred A. Knopf 1945, copyright 1934 by Alfred A. Knopf, Inc.

DOI: 10.1175/JAS-D-20-0312.1

Forecasts (ECMWF) (ERA5; Hersbach et al. 2020) for the selected time period. Currently, the high-resolution deterministic forecasts (HRES) of the IFS provide predictions with a horizontal resolution of about 9 km globally in a model domain extending up to 80-km altitude. These forecasts have a high skill in the troposphere and in the stratosphere (Preusse et al. 2014; Bauer et al. 2015; Le Pichon et al. 2015; Ehard et al. 2018; Dörnbrack et al. 2017). ERA5 provides hourly estimates of atmospheric variables. The data cover Earth on a 30-km grid and resolve the atmosphere using 137 hybrid levels from the surface up to a height of 80 km. Although ERA5 has a coarser resolution than the HRES products for the considered time period January 2016, it still resolves the dominant modes with horizontal wavelength greater than 100 km that are important for this study. Additionally, ERA5 forecasts provide the parameterized tendencies of the zonal and meridional winds. Both fields will be used to estimate and quantify the wave drag induced by the stratospheric gravity waves.

The following material is presented in five sections. Section 2 overviews the tropospheric and stratospheric ambient flow conditions for the case study during the selected time period. Different criteria for the excitation of internal gravity waves are inspected in section 3. The subsequent section 4 investigates the properties of the stratospheric gravity waves over Northern Europe. Section 5 discusses the generic flight tracks, the stratospheric wave drag associated with the gravity wave event, and finally, section 6 concludes this study.

2. Atmospheric background flow conditions

a. Tropospheric flow

Figure 1 shows a snapshot of the mean sea level pressure and the equivalent potential temperature on the 850-hPa pressure surface at 1200 UTC 12 January 2016. Animations of the temporal evolution of both quantities from 11 to 13 January 2016 based on 1-hourly ERA5 data can be found in the online supplementary material. A deep low with minimum core pressure of about 980 hPa was located over the United Kingdom at 1200 UTC 11 January 2016 and, afterward, it propagated eastward and a second low over Russia appeared (Fig. 1a). At this time, extremely large pressure gradients developed on its eastern edge that extended north–south at around 40°E over Russia. These large gradients were associated with the frontal systems that intensified during the period (Fig. 1b). Finally, the cyclogenesis resulted in a warm front progressing east and north and a cold front trailing behind it (see Fig. 1b).

As a result of this synoptic development, strong low-level westerly winds greater than 10 m s^{-1} prevailed in a broad band south of about 50°N as exemplified by the horizontal wind magnitude V_H at the 700-hPa pressure level in Fig. 2a. East of 30°E, the low-level winds became more southerly. The polar-front jet at 300 hPa had developed above a region of enhanced middle- and lower-tropospheric baroclinicity, the polar front as seen in Fig. 1b. This upper-level jet streak had a large alongstream extent and was nearly zonally oriented at 45°N and

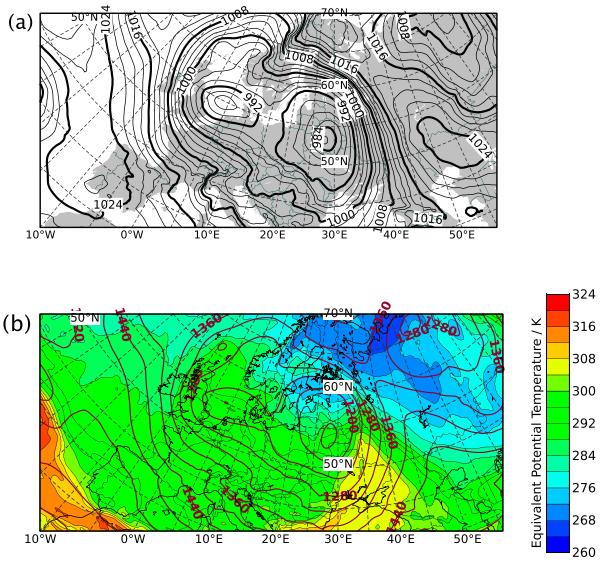

FIG. 1. (a) Mean sea level pressure (hPa, solid lines) and (b) equivalent potential temperature (K, color shaded) and geopotential height (m, gray solid lines) on the 850-hPa pressure surface at 1200 UTC 12 Jan 2016. Animations of the plotted fields are provided for the period 10–13 Jan 2016 in the online supplemental material.

$V_H > 70$ m s^{-1} in its core (Fig. 2b). During the considered period, the polar-front jet bent and advanced southward in conjunction with the deepening upper-level trough. Similar to the low-level winds, also the exit region of the jet obtained a more southerly component between 30° and 40°E (Fig. 2b). The deepening of the upper-level trough and downstream ridge building over Russia are clearly visible in the tropopause map (Morgan and Nielsen-Gammon 1998) as shown in Fig. 2c. The large slope of the tropopause height toward south is related to the strong zonal winds of the upper-level jet (Shapiro and Keyser 1990).

b. The Arctic polar vortex

The evolution of the stratospheric polar vortex in the Northern Hemispheric winter 2015/16 has been investigated by a series of papers: Matthias et al. (2016), Manney and Lawrence (2016), Dörnbrack et al. (2017), and Voigt et al. (2018). The Arctic polar vortex was very stable and extremely cold in the early phase until end of December 2015. Afterward, planetary wave activity displaced the vortex off the pole and weakened its strength (see the appendix). The period in the middle of January 2016 belongs to one of the early planetary wave disturbances shifting the vortex center toward Iceland.

The temporal evolution of the 10-hPa absolute temperature T and horizontal wind V_H at two selected meridians as function of latitude is illustrated in the Hovmöller plots of Fig. 3. After the poleward shift of the cold pool during the first week of January 2016 (not shown), the temperature distribution was nearly stationary at 10°E during the considered time period and cold air was located north of about 60°N

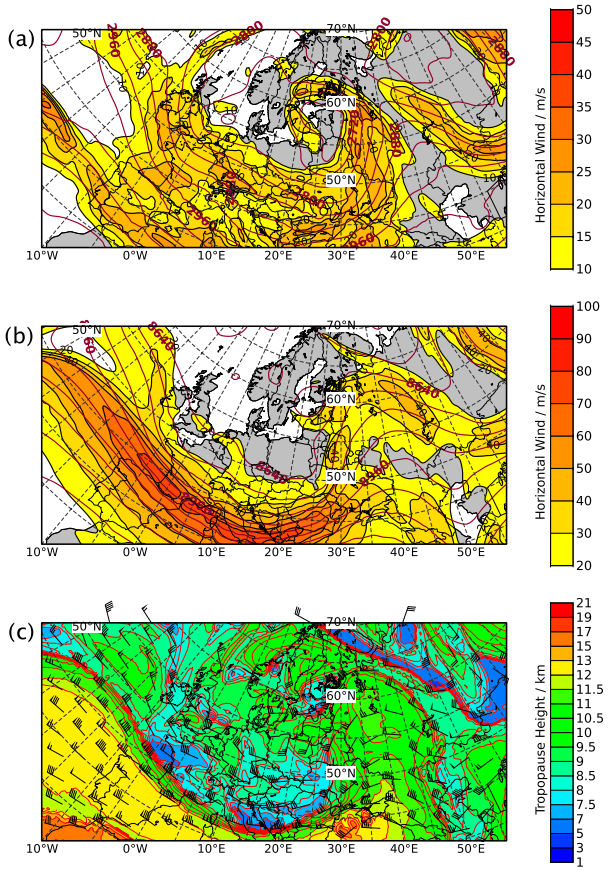

FIG. 2. Horizontal wind V_H (m s^{-1}, color shaded) and geopotential height (m, solid lines) at (a) 700 and (b) 300 hPa and (c) tropopause height (km, color shaded) at 1200 UTC 12 Jan 2016. Barbed symbols in (c) are V_H with half barb = 2.5 m s^{-1}, full barb = 5 m s^{-1}, and pennant = 25 m s^{-1}. Animations of the plotted fields are provided for the period 10–13 Jan 2016 in the online supplemental material.

(Fig. 3a). Farther east at 50°E, the slow poleward retreat of cold air (10°/48 h ≈ 6.5 m s^{-1}) due to the vortex displacement was still ongoing (Fig. 3b). At 10°E, the core of the polar night jet (PNJ) at 10 hPa was located slightly south of 55°N whereas at 50°E the PNJ propagated northward in accordance with the progression of the cold pool of the Arctic polar vortex (Figs. 3c,d). The different behaviors at 10° and 50°E reflect the deformation and zonal elongation of the Arctic polar vortex.

Figure 4 displays V_H at three stratospheric pressure surfaces for 1200 UTC 12 January 2016. Compared to the tropopause jet (Fig. 2b) the PNJ is located at higher latitudes and the nearly zonally oriented strong flow ($V_H > 120$ m s^{-1}) spreads across Europe. The pressure levels shown in Fig. 4 encompass local V_H maxima of the PNJ resembling the entrance and exit regions of a jet streak. At 1 and 5 hPa the jet streak appears to be stronger disturbed by mesoscale perturbations leading to undulations in V_H and in geopotential height Z. The axis of the PNJ was tilted poleward; i.e., V_H was larger at higher levels and latitudes. This poleward tilt is illustrated for the 10° and 50°E meridians in Fig. 5 and resulted from the preceding vortex displacement. Thus, the stratospheric wind distribution at this time period differs substantially from the equatorward tilt of the PNJ generally found in climatological means (see Schoeberl and Newman 2015).

3. Conditions for gravity wave excitation

a. Low-level forcing

Low-level winds of magnitudes as shown in Fig. 2a are known to excite mountain waves. Usually, one assumes wind speeds V_H in excess of 10 m s^{-1} at the crest of the ridge. The wind direction α_H should be within a sector of $\pm 30°, \ldots, 45°$ to the normal of the ridge of high ground. To allow for the favorable vertical propagation, V_H should increase with altitude and α_H should only marginally turn over a significant height band (Dörnbrack et al. 2001; Alexander et al. 2013).

Figure 6 depicts the main European mountain ranges and outlines eight control areas. The time series of V_H and wind direction α_H at 700 hPa as shown in Fig. 7 document the evolution of the low-level flow inside the respective control areas. In the early phase of the considered period, $V_H > 20$ m s^{-1} occurred over France and Central Europe. In the time series, the V_H maximum progressed successively eastward; i.e., first, there was a strong flow across the Pyrenees, then the Alps and the Apennines, and, finally, past the Dinaric Alps (Fig. 7a). In these areas, V_H decreased gradually during the second half of the period. Westerlies dominated the wind in the control areas except for Scandinavia where weaker winds turned cyclonically from southerlies to easterlies and northerlies. At the same time, a more southerly component of V_H prevailed over Russia in association with the evolving low (Fig. 1a). Summarizing, this broad band of high low-level winds was able to excite vertically propagating gravity waves at the various European mountain ranges.

b. Spontaneous gravity wave emission

To quantify if nonorographic internal gravity waves could have been excited by spontaneous emission either from the polar-front jet or from the PNJ, simple common criteria as those described by Zhang et al. (2000) and Plougonven and Zhang (2014) are reviewed. The display of the horizontal divergence $\delta = \partial u/\partial x + \partial v/\partial y$ is often used to emphasize unbalanced motions in form of alternating patterns of positive and negative δ values (Plougonven and Teitelbaum 2003). In Fig. 8a, a small lower threshold of $\delta = 0.5 \times 10^{-4}$ s^{-1} is applied to visualize δ. Dörnbrack et al. (2012) and Khaykin et al. (2015) used $\delta = 1 \times 10^{-4}$ s^{-1} above which significant wave amplitudes in temperature are to be expected. Figure 8a reveals small values ($|\delta| < 1 \times 10^{-4}$ s^{-1}) at 300 hPa and even smaller values at pressure levels above (not shown). Also, animations of δ do not reveal larger magnitudes at times before or after the one shown in Fig. 8a.

The Rossby number Ro = $U/(Lf)$ measures the separation of two time scales: balanced motions evolve on the advective time scale L/U, whereas the longest time scale for gravity wave motions is $1/f$, with f the Coriolis parameter

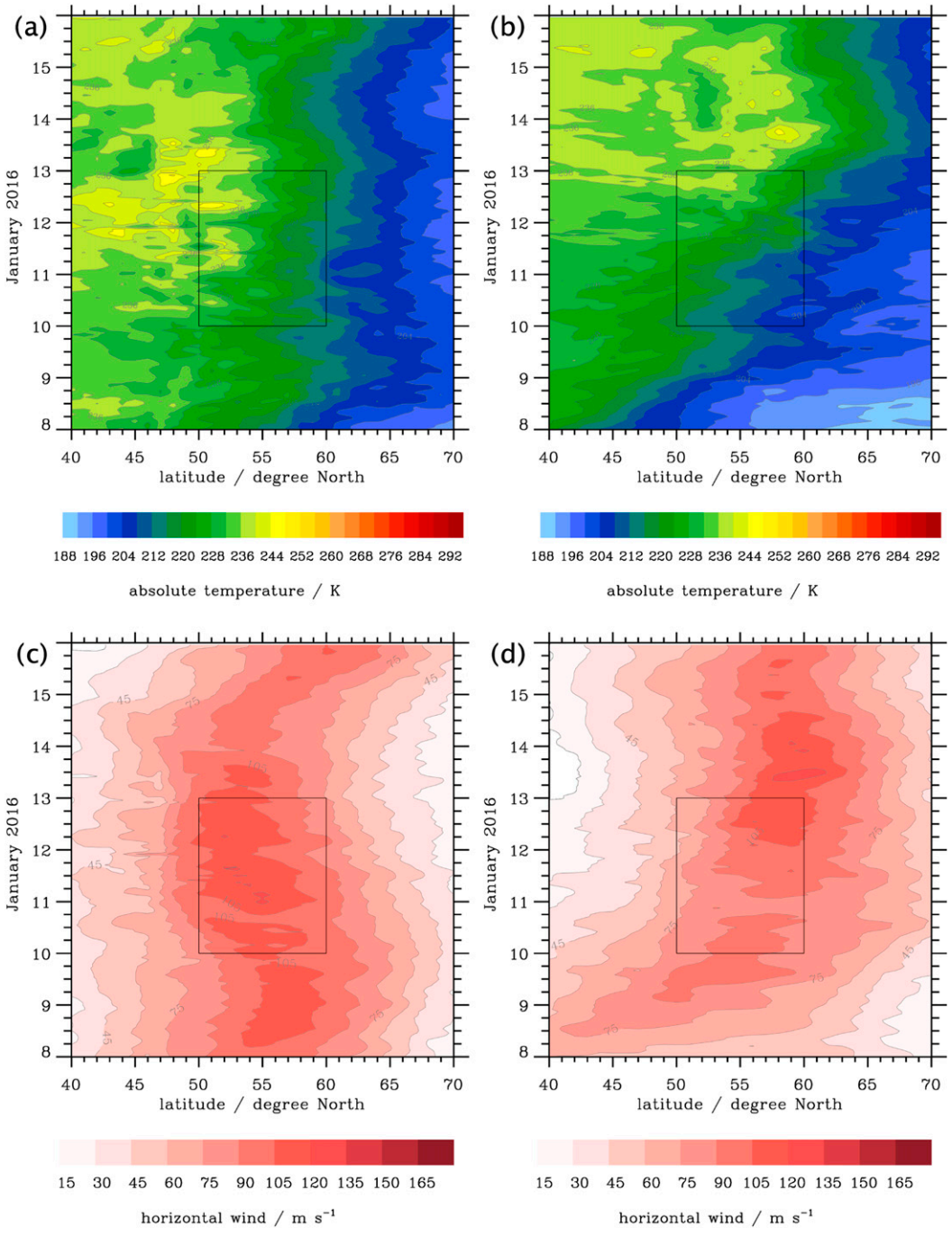

FIG. 3. Temporal evolution of the (top) 10-hPa absolute temperature (K, color shaded) and (bottom) horizontal wind V_H (m s^{-1}, color shaded; $\Delta V_H = 15\,\mathrm{m\,s^{-1}}$) at (a),(c) 10° and (b),(d) 50°E.

(Pedlosky 1987). Rossby numbers are typically small for midlatitude flows. To a very good approximation, atmospheric motions at small Rossby numbers are balanced; i.e., a diagnostic relation can be established between the wind and other variables (Vallis 2017). Estimates of the Rossby number Ro calculated with $L = 1400$ km as approximate distance between the upper level trough and ridge and the maximum wind speed in the jet core $U = 80\,\mathrm{m\,s^{-1}}$ result in values of Ro ≈ 0.48 for the situation shown in Figs. 8b and 2b.

Figure 8b shows the local Rossby number $\mathrm{Ro}_\zeta = \zeta/f$ calculated with the relative vorticity $\zeta = \partial v/\partial x - \partial u/\partial y$ as measure for the inverse advective time scale. At this time, enhanced values $\mathrm{Ro}_\zeta \approx 0.8$ are found slightly east to the trough axis extending into the jet exit region. Figure 9a depicts the temporal

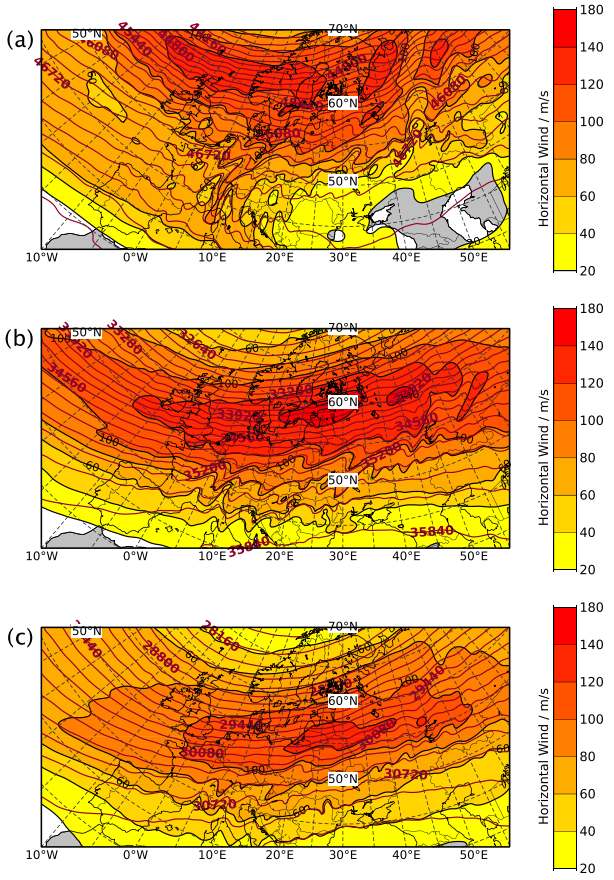

FIG. 4. Horizontal wind V_H (m s^{-1}, color shaded) and geopotential height (m, solid lines) at (a) 1, (b) 5, and (c) 10 hPa at 1200 UTC 12 Jan 2016.

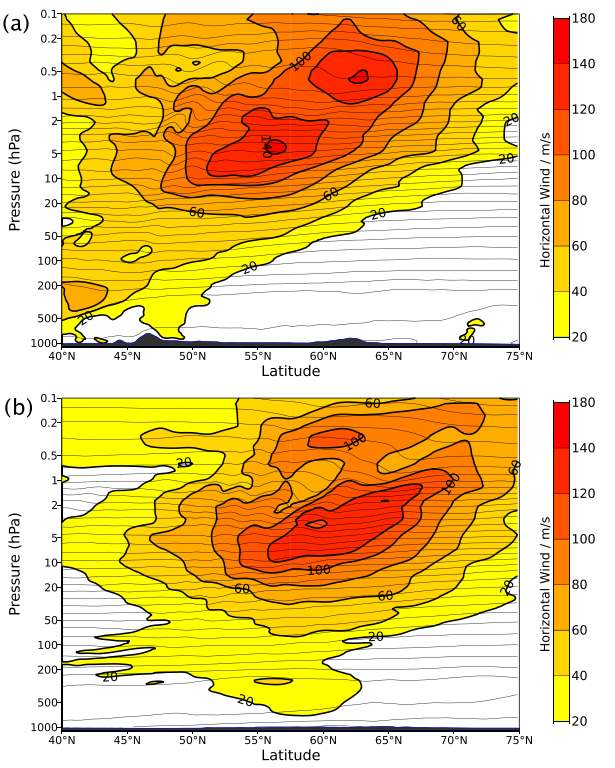

FIG. 5. Horizontal wind V_H (m s^{-1}, color shaded) along the (a) 10° and (b) 50°E meridians at 1200 UTC 12 Jan 2016. The thin solid lines are isentropes in logarithmic scaling.

evolution of Ro_ζ for selected control areas during January 2016 based on hourly ERA5 data. Here, Ro_ζ values larger than 0.5 are computed for the control area Pyrenees, Alps, and Middle Europe during the period from 10 to 13 January 2016, but the values never exceed 1. As already mentioned by Wang et al. (2009), enhanced local Rossby number are associated with regions inside the vortex cores. Therefore, the temporal evolution of Ro_ζ does reflects the passages of upper level troughs but does not appear to be suitable to quantify the potential of spontaneous gravity wave emission.

The cross-stream Lagrangian Rossby number $\mathrm{Ro}_\perp = |\mathbf{V}_{\mathrm{ag}}^{\perp}|/V_H$ constitutes another indicator of unbalanced motions (Koch and Dorian 1988) and a horizontal plot of $\mathrm{Ro}_\perp$ at 300 hPa is shown in Fig. 8c. Here, $\mathbf{V}_{\mathrm{ag}}^{\perp}$ is the ageostrophic wind vector perpendicular to the horizontal wind vector $\mathbf{V}$. Values of $\mathrm{Ro}_\perp$ were calculated for $V_H > 10\,\mathrm{m\,s^{-1}}$, otherwise the small denominator generates spuriously large $\mathrm{Ro}_\perp$ (see Tateno and Sato 2008). The jet exit region shows enhanced values but leaves $\mathrm{Ro}_\perp$ smaller than 0.4 during the period from 10 to 13 January 2016. Tateno and Sato (2008) relate values larger 0.6 to source regions for spontaneously emitted inertia–gravity waves. The time series in Fig. 9b also confirm the smallness of the cross-stream Lagrangian Rossby number $\mathrm{Ro}_\perp$ for the selected control areas.

Furthermore, the residual of the nonlinear balance equation ΔNBE (Zhang et al. 2000) is calculated for the ERA5 data according to

$$\Delta\mathrm{NBE} = 2J(u,v) + f\zeta - \nabla^2\Phi - \beta u, \qquad (1)$$

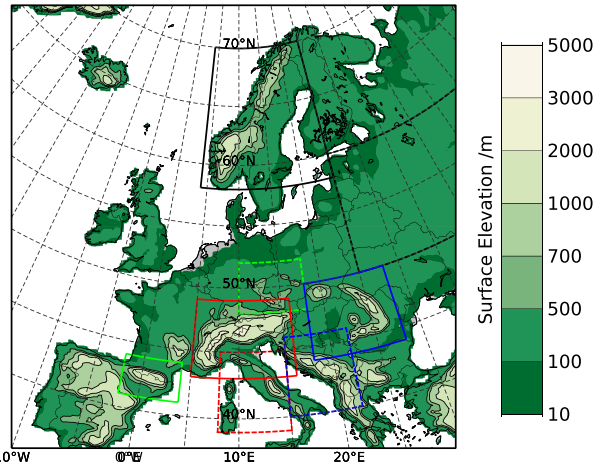

FIG. 6. Surface elevation (m, color shaded) and eight control areas: solid red: Alps; dashed red: Apennines; solid green: Pyrenees, dashed green: Middle European mountain ranges; solid blue: Carpathians; dashed blue: Dinaric Alps; solid black: Scandinavian mountains; dashed black: Russia.

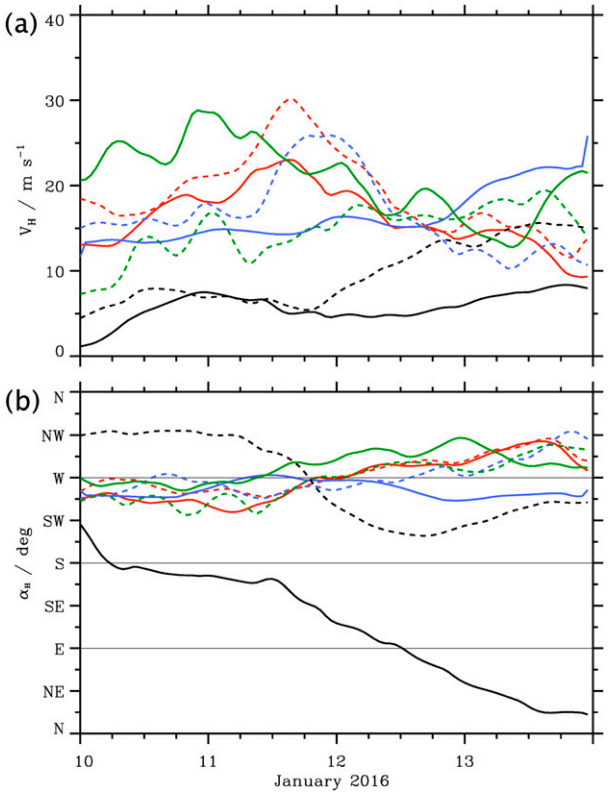

FIG. 7. (a) Horizontal wind V_H and (b) wind direction α_H at 700 hPa as area averages for the eight control areas as defined in Fig. 6. The line style is the same as used for plotting their circumferences in Fig. 6.

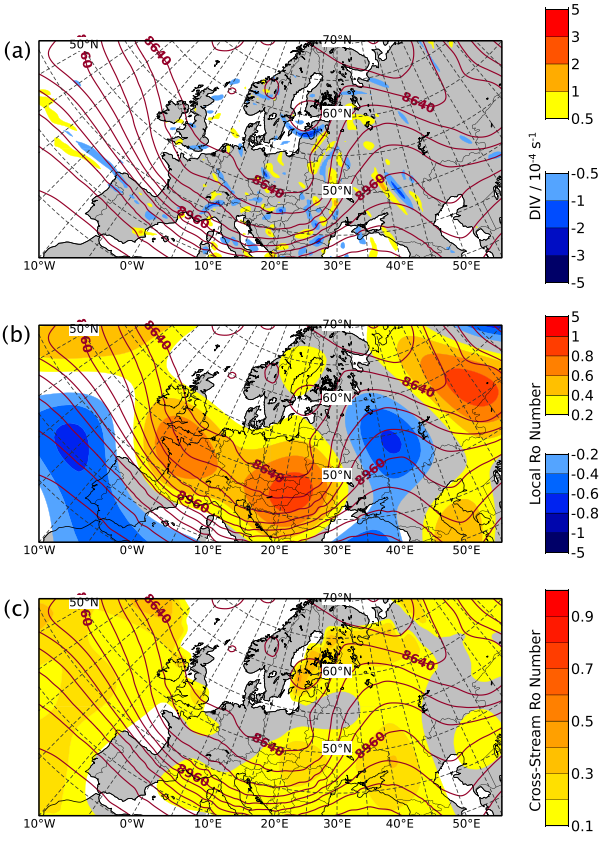

FIG. 8. (a) Horizontal divergence δ (10^{-4} s^{-1}, color shaded), (b) local Rossby number Ro_ζ, and (c) cross-stream Lagrangian Rossby number $\mathrm{Ro}_\perp$ at 300 hPa at 1200 UTC 12 Jan 2016. Solid lines are geopotential height. The quantities δ, Ro_ζ, and $\mathrm{Ro}_\perp$ are retrieved from ERA5 with different spectral resolutions: δ is retrieved using all available spectral coefficients and interpolated on a regular 0.281 25° × 0.281 25° latitude–longitude grid, while Ro_ζ and $\mathrm{Ro}_\perp$ are retrieved for all horizontal wavenumbers less than 21 and interpolated on a 2.5° × 2.5° grid. An animation of the plotted horizontal divergence is provided for the period 10–13 Jan 2016 in the online supplemental material.

where Φ is the geopotential, $\beta = \partial f/\partial y$, and J denotes the Jacobian. For pressure levels of 300 and 200 hPa around the polar-front jet ΔNBE rarely exceeds 2×10^{-9} s^{-2}; see the temporal evolution for the 300 hPa level in Fig. 9c. Zhang et al. (2001) used values larger than 1×10^{-8} s^{-2} as indicator of strongly unbalanced flow able to emit gravity waves spontaneously. Therefore, the really small values of |ΔNBE| support the previous findings using δ, Ro, Ro_ζ, and $\mathrm{Ro}_\perp$ for diagnosing flow imbalance. Based on these results ($|\delta| < 1 \times 10^{-4}$ s^{-1}, $\mathrm{Ro} < 0.5$, $\mathrm{Ro}_\zeta < 1$, $\mathrm{Ro}_\perp < 0.5$, and $|\Delta\mathrm{NBE}| < 1 \times 10^{-8}$ s^{-2}), it appears unlikely that spontaneous emission of nonorographic gravity waves from the polar-front jet played a central role.

Figure 10 shows enhanced absolute values of ΔNBE ≈ 4×10^{-9} s^{-2} at three stratospheric levels indicating that the unbalanced PNJ might be a source of gravity waves. |ΔNBE| values of the same order of magnitude were shown by Sato and Yoshiki (2008) occurring at the inner edge of the PNJ. Here, enhanced values of |ΔNBE| occur both at the inner as well as the equatorward side of the PNJ. Area-averaged |ΔNBE| values for the considered time period are shown in Fig. 11. Similarly to the tropospheric 300 hPa level, the stratospheric |ΔNBE| values are smaller than 1×10^{-8} s^{-2}; however, during the period from 10 to 13 January 2016 |ΔNBE| is systematically enhanced to about 4×10^{-9} s^{-2} in all selected control areas compared to the times before and toward the end of January 2016. This opens the faint possibility that gravity waves were spontaneously emanating from these regions, a scenario discussed by Bossert et al. (2020).

c. *Inertial instability*

There is a large positive meridional gradient $\partial u/\partial y$ at the equatorward, anticyclonic side of the PNJ (Fig. 4). Here, this strong anticyclonic shear may lead to negative values of the absolute vorticity $\zeta + f$. As outlined by Rowe and Hitchman (2015), negative values of absolute vorticity can be used as reliable indicator of inertial instability (Dutton 1976; Knox 2003). The resulting parcel's inertial acceleration generates enhanced small-scale motions such as turbulence and internal gravity waves can be radiated from these regions (e.g., Arakawa 1952; Knox 1997; Rowe and Hitchman 2015).

Figure 12 shows the absolute vorticity at 5 hPa at 1200 UTC 12 January 2016 for three different kinds of ERA5 retrievals.

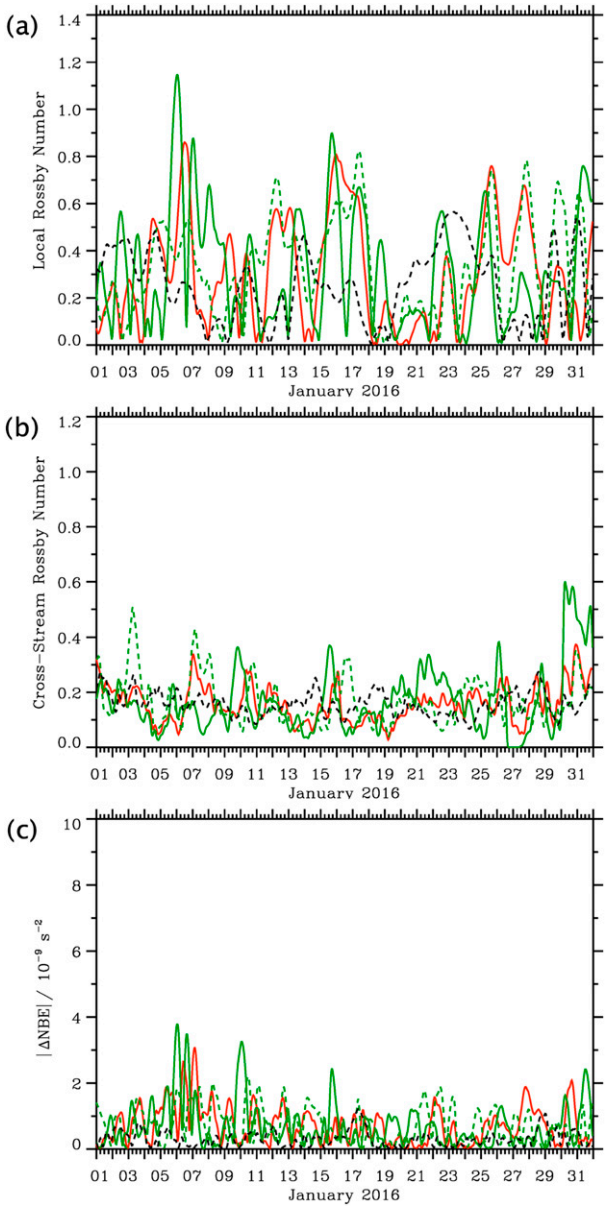

FIG. 9. Temporal evolution of the area-averaged (a) local Rossby numbers Ro_{ζ}, (b) the cross-stream Rossby numbers $\mathrm{Ro}_{\perp}$, and (c) the residuals of the nonlinear balance equation |ΔNBE| for selected control areas at 300 hPa. The line style is the same as used for plotting their circumferences in Fig. 6.

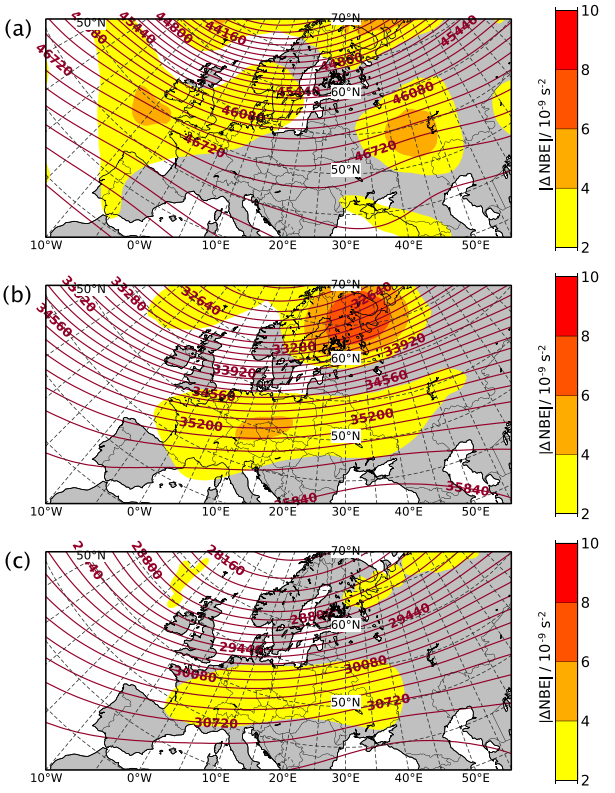

FIG. 10. Residuals of the nonlinear balance equation |ΔNBE| ($10^{-9}\,\mathrm{s}^{-2}$, color shaded) at (a) 1, (b) 5, and (c) 10 hPa at 1200 UTC 12 Jan 2016. Solid lines are geopotential height. The quantities for computing ΔNBE are retrieved for all horizontal wavenumbers less than 21 and interpolated on a 2.5° × 2.5° latitude–longitude grid.

Figure 12a displays the absolute vorticity in full spectral resolution interpolated on the native ERA5 grid with 0.281 25° resolution in latitude and longitude. Large positive values dominate the center of the polar vortex whereas much smaller and even negative values are simulated in the vicinity of the edge of the polar vortex. The negative areas appear as filamentary structures expanding downwind. The same field interpolated on a regular 2.5° grid is shown in Fig. 12b and the plotted structures are smooth compared to the previously shown field while maintaining their overall appearance. Finally, Fig. 12c displays the absolute vorticity retrieved with truncated spectral resolution mimicking the output of a coarse-resolution general circulation model that does not contain mesoscale modes. Again, the meridional gradient is reproduced; however, no negative values but only small positive values of around $10^{-5}\,\mathrm{s}^{-1}$ are found.

The negative values as identified in Figs. 12a and 12b are located directly above the European continent and only appear in the data containing mesoscale motion modes. Therefore, they can be most probably attributed to vertically propagating internal gravity waves resolved by ERA5 (see next section). Thus, the large-scale stratospheric flow field does not seem to be inertially unstable and these regions can be excluded as a stratospheric source of gravity waves.

4. Stratospheric gravity wave fields

a. Overview

We begin our journey through the stratospheric gravity waves occurring during the considered period by visualizing temperature perturbations T'. The perturbations T' are calculated as differences between the temperatures from hourly

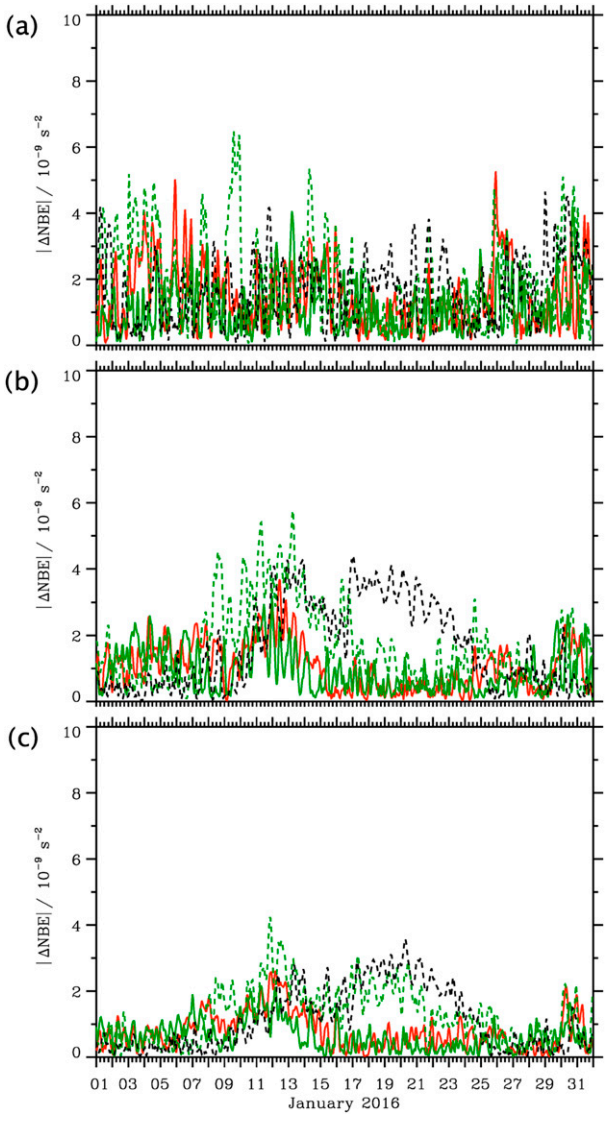

FIG. 11. Temporal evolution of the area-averaged residuals of the nonlinear balance equation |ΔNBE| for the different control areas at (a) 1, (b) 5, and (c) 10 hPa. The line style is the same as used for plotting their circumferences in Fig. 6.

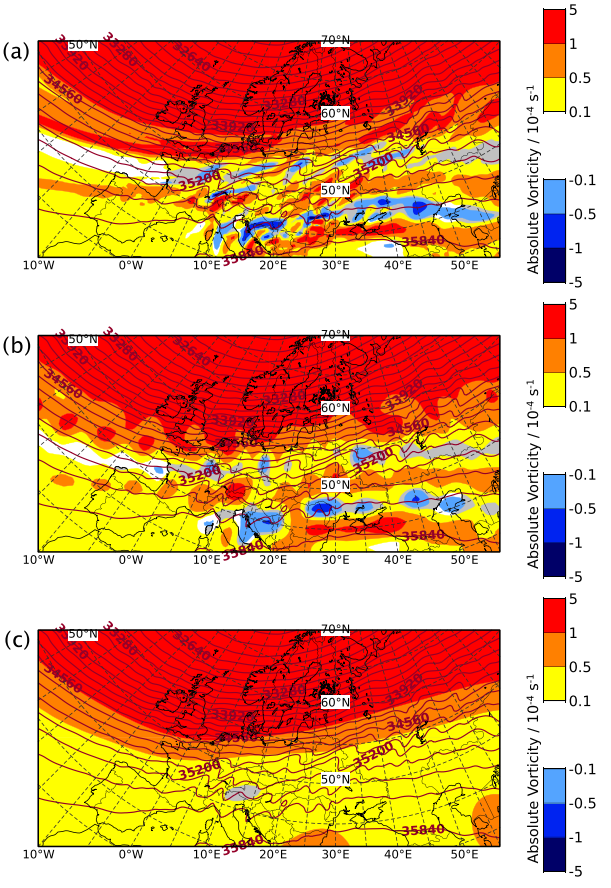

FIG. 12. Absolute vorticity ($10^{-4}\,s^{-1}$, color shaded) at 5 hPa at 1200 UTC 12 Jan 2016. Solid lines are geopotential height. (a),(b) The quantities retrieved with full spectral resolution of the ERA5 data and interpolated on a (a) 0.281 25° × 0.281 25° and (b) 2.5° × 2.5° latitude–longitude grid. (c) The absolute vorticity retrieved for all horizontal wavenumbers less than 21 and interpolated on a 2.5° × 2.5° grid.

ERA5 data retrieved at full spectral resolution T639 and spectrally truncated fields at T106 interpolated on the same 0.25° × 0.25° regular latitude–longitude grid. Perturbations associated with horizontal wavenumbers 106 and higher represent scales of about 200 km down to the effective resolution of the ERA5. Therefore, the total horizontal wavenumber 106 is chosen as it can be used to distinguish between synoptic-scale and mesoscale modes as due to inertia–gravity waves (Žagar et al. 2017; Schumann 2019). In this sense, positive and negative T' values can be associated with troughs and crests, i.e., with the phases of internal gravity waves.

Figure 13 exemplifies the T' fields at three stratospheric pressure levels—at the 1-, 5-, and 10-hPa pressure surfaces, i.e., at about 45–30-km altitude—for 1200 UTC 12 January 2016. As can be seen in the supplementary animations, the outbreak of stratospheric wave activity occurred after 10 January 2016 at around 1200 UTC. Elongated wave fronts appeared subsequently all over Europe. Apparently, the waves originated from the flow over the Central European mountain chains ranges located at around 45°N. From there, they extendedto the northeast. If this hypothesis holds up it would imply a horizontal advection of wave momentum and wave energy by about 2500 km from the excitation at the European mountain ranges to their upper-stratospheric arrival over Russia.

The phases of the wave fronts appear nearly coherent in Fig. 13. However, their varying T' magnitudes and gaps indicate different sources, wave packets launched at subsequent times, and wave packets possessing different propagation histories. In spite of their different, individual propagation pathways, the most straightforward explanation is that the mountain waves as seen in Fig. 13 propagated along oblique paths, crossing higher pressure levels consecutively at greater latitudes.

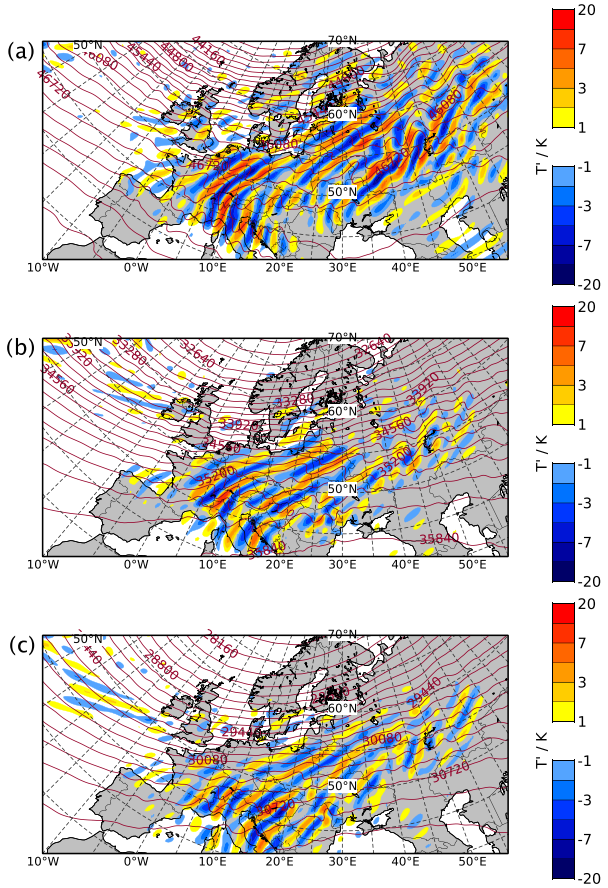

FIG. 13. Temperature perturbations T' (K, color shaded) and geopotential height (m; solid lines) at (a) 1, (b) 5, and (c) 10 hPa at 1200 UTC 12 Jan 2016. Animations of the plotted fields are provided for the period 10–13 Jan 2016 in the online supplemental material.

Figures 14 and 15 complement the overview by displaying vertical cross sections of T' along two meridians and two circles of latitude, respectively. The common feature of the gravity waves plotted at the western and eastern meridians is their vertical, northward tilt from low latitudes into the PNJ at higher ones (Fig. 14). Whereas the waves are connected to T' patterns in the troposphere and lower stratosphere at the western meridian (Fig. 14a), they only occur at stratospheric levels along the eastern meridian (Fig. 14b). A further indication of the vertical tilt of the gravity waves is provided by Fig. 15. There, gravity wave signatures only appear at stratospheric levels along the northern cross section (Fig. 15b). The southern section (Fig. 15a) reveals tropospheric as well as stratospheric T' patterns directly above the different mountain chains. Consulting the supplementary animations reveals that the stratospheric gravity waves are due to the flow past the mountains: the phase lines are quasi stationary during certain periods and show typical mountain wave patterns (e.g., inclining against the westerly winds) propagating from the troposphere to the stratosphere. In contrast, the northern section as displayed in Fig. 15b only reveals gravity waves above about 30 hPa. These waves are confined in regions where $V_H > 80\,\mathrm{m\,s^{-1}}$.

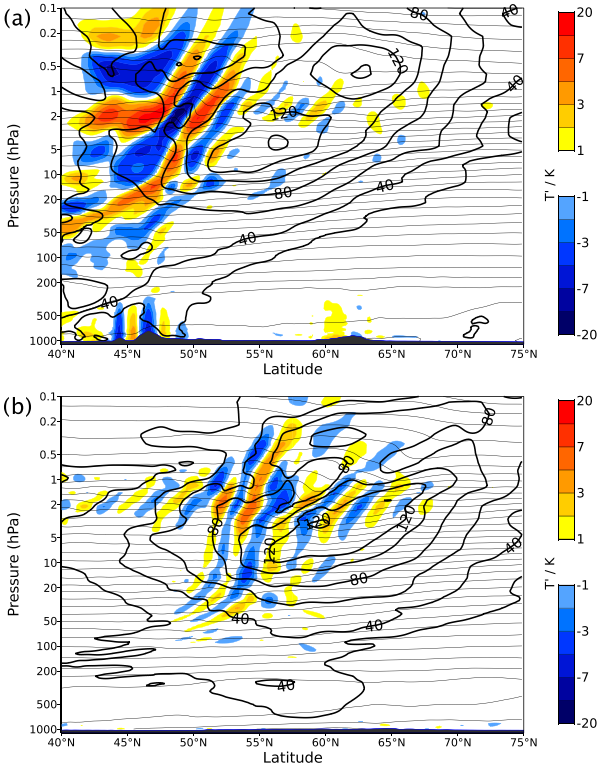

FIG. 14. Temperature perturbations T' (K, color shaded) and horizontal wind V_H (m s^{-1}, solid lines) along the (a) 10° and (b) 50°E meridians at 1200 UTC 12 Jan 2016. The thin solid lines are isentropes with logarithmic scaling. Animations of the plotted fields are provided for the period 10–13 Jan 2016 in the online supplemental material.

b. *Dependence on forecast lead time*

The question might arise if the stratospheric waves in the ERA5 data as presented before were imprinted by the data assimilation system as the ECMWF uses satellite radiances to constrain stratospheric temperatures (see Polichtchouk et al. 2021). For answering this question, Fig. 16 exemplifies the stratospheric wave field at 1 hPa valid at 1200 UTC 12 January 2016 for IFS predictions by the HRES model for lead times of 0 h (equivalent to the operational analysis), 72 h, and 144 h, respectively. At all lead times, the stratospheric gravity waves show similar patterns as the ERA5 results as displayed in Fig. 13a. Although there are differences in the details of the numerical integration results, the similar patterns at all lead times indicate that they were not enforced by the assimilated satellite data but result from resolved processes in the IFS integration. This finding is in line with the results of Eckermann et al. (2019) that gravity waves in the analysis originate almost entirely from model-generated waves in the high-resolution forecasts backgrounds.

c. *Wave characteristics*

The horizontal and vertical wavelengths λ_H and λ_Z of the stratospheric gravity waves were estimated from Figs. 13–15. The horizontal wavelength varies between 210 and 325 km

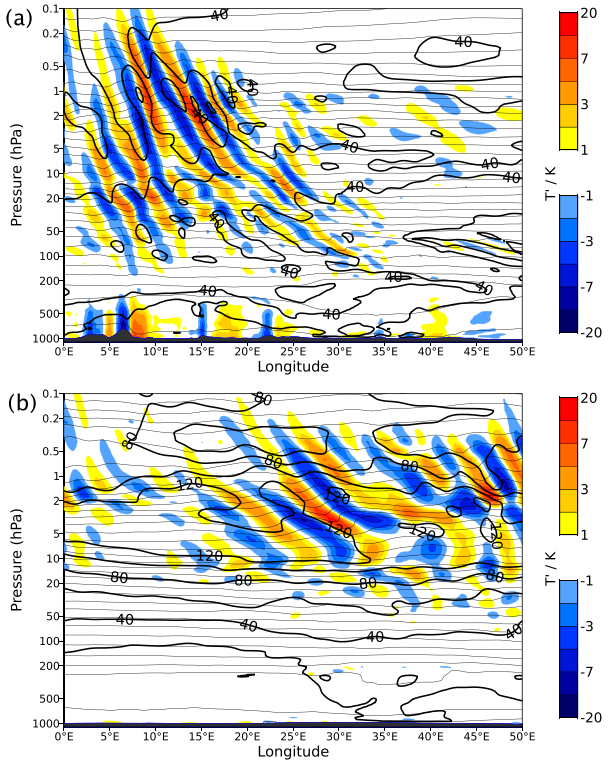

FIG. 15. Temperature perturbations T' (K, color shaded) and horizontal wind V_H (m s^{-1}, solid lines) along the (a) 45° and (b) 55°N circles of latitude at 1200 UTC 12 Jan 2016. The thin solid lines are isentropes in logarithmic scaling. Animations of the plotted fields are provided for the period 10–13 Jan 2016 in the online supplemental material.

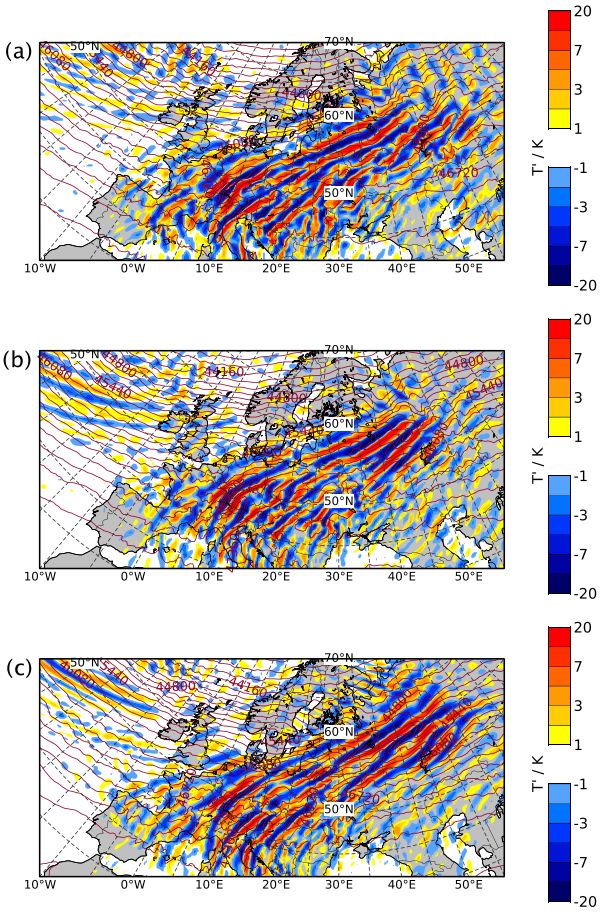

FIG. 16. Temperature perturbations T' (K, color shaded) and geopotential height (m, solid lines) at 1 hPa and the valid time of 1200 UTC 12 Jan 2016 for different forecast lead times of the operational IFS: (a) 0 h = operational analysis, (b) +72 h, and (c) +144 h.

whereby the longer λ_H values occur at higher levels and further to the northeast. The value of λ_Z over the mountains is about 18 ± 2 km (Fig. 14). All estimates refer to pressure levels higher than 50 hPa. Although the operational analyses have a higher horizontal resolution (about 9 km), λ_H values as estimated from Fig. 16 do not deviate strongly from the ones obtained by the ERA5 data; here, λ_H varies between 260 and 340 km. To investigate the phase propagation of the simulated gravity waves, Hovmöller diagrams of the T' fronts are plotted for three different circles of latitude and at two stratospheric pressure levels (Fig. 17). Generally, the phase lines reveal stationary, quasi-stationary, and nonstationary modes.

At 47°N, stationary modes exist east of the Greenwich meridian and extend up to 20°E both at 1 and 10 hPa (Figs. 17a,d). The appearance of these stationary modes is associated with the strong winds over the Pyrenees and the increase of the low-level wind speed over the control area Alps (see the green and red solid lines in Fig. 7a). The amplitude varies as function of time but no indications of overturning or saturation exists. Thus, the mountain waves do not encounter critical levels and propagate quasi linearly into the middle atmosphere. Here, mountain waves excited by the flow past isolated peaks with phase fronts nearly parallel to the incoming flow mainly propagate vertically. Their wave energy will be found directly above the respective mountains. In contrast, mountain waves with phase fronts inclined to the flow will propagate upward, outwards, and downstream (see Smith 1980; Eckermann et al. 2015). The horizontal geometrical spreading of these essentially hydrostatic mountain waves lead to a superposition of modes excited by different mountain peaks and ridges. Thus, not every wave train in the middle atmosphere is connected to a topographic feature directly underneath. Whereas the stationary period at 10 hPa lasts from about 0600 UTC 11 January until 1200 UTC 13 January 2016, mountain waves appear at 1 hPa slightly later reflecting the finite propagation time into the upper stratosphere.

Further north at 52°N, stationary waves exist at the upper pressure level (Fig. 17b). The slightly tilted phases at 10 hPa (Fig. 17e) might also results from mountain waves propagating in a slowly varying background flow (cf. Fig. 3c). The meridional extent of the stationary modes is similar to the ones identified further south and they last 48 h starting at 0000 UTC

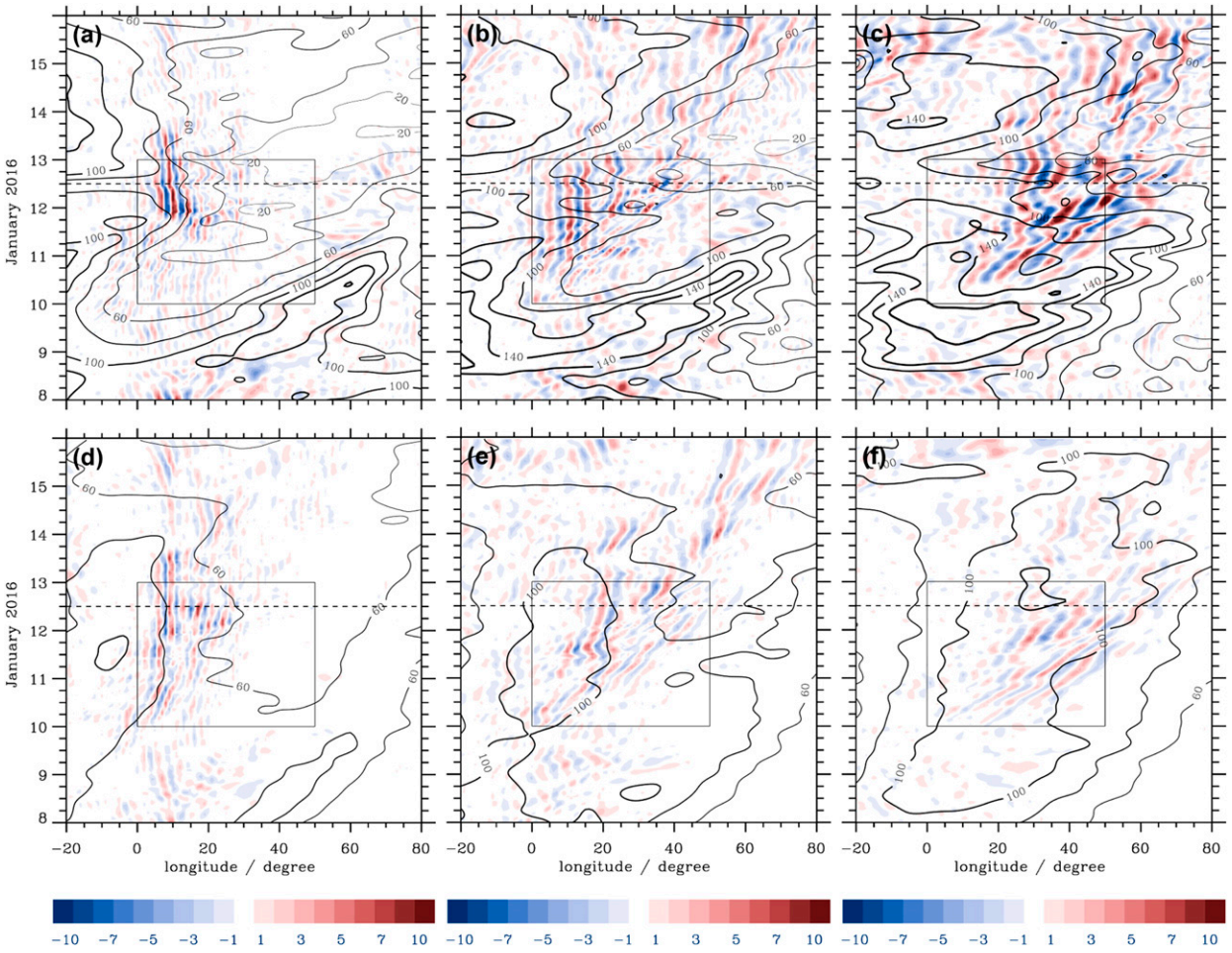

FIG. 17. Temperature perturbations T' (K, color shaded) and horizontal wind V_H (m s^{-1}, black contour lines of increasing thickness every 20 m s^{-1}) at (a)–(c) 1 and (d)–(f) 10 hPa as function of time for (a),(d) 47°, (b),(e) 52°, and (c),(f) 57°N. The dashed lines denote 1200 UTC 12 Jan 2016. The box encloses the considered period and the area of interest from the Greenwich meridian to 50°E.

11 January 2016. These stationary and quasi-stationary modes are generated by the oblique horizontal propagation of the mountain waves excited by the flow over the Alps as suggested by the coherent appearance of the bent phase lines as shown in Fig. 13.

At the northernmost latitude circle at 57°N, nearly stationary modes can only be detected at 1 hPa and they appear at late times after 1200 UTC 12 January 2016 lasting about 24 h (Fig. 17c). Although the phase lines are not strictly straight, the wave packets centered at about 0000 UTC 13 January appear coherent and their slight zonal meandering might result from transient background conditions where the waves were propagating through (cf. Fig. 3d). The zonal extent is much larger compared to the lower latitudes and they spread up to 50°E. At lower stratospheric levels of 10 hPa, propagating modes dominate (Fig. 17f).

The horizontal wind V_H is added in Fig. 17. Whereas V_H ranges from 60 and 120 m s^{-1} at 10 hPa and varies only marginally with time (see Figs. 3c,d), V_H at 1 hPa is drastically reduced by up to 40 m s^{-1} day^{-1} during the mountain wave event. This value is an estimate from the V_H reduction as shown in Fig. 17c; see the discussion of the stratospheric wave drag in section 5.

Consulting the animations of the 1-hourly output of T' at 1-hPa different wave packets can be identified: some of them appear nearly stationary over the Alps or other mountain ranges. Their amplitudes vary in time, yet their positions remain nearly the same. In some periods, nonstationary phase lines indicate waves resulting from excitation under transient low-level flows (see Fig. 7a). Another transience is introduced by the wave–mean flow interaction due to the momentum deposition by the gravity waves as documented by the reduction of V_H.

Nevertheless, the overall impression from the Hovmöller plots in Fig. 17 and the animations is the quasi stationarity of stratospheric gravity waves even at locations far north. This result points to mountains as the dominant source of the stratospheric gravity waves. Furthermore, all wave packets share the same meridional spreading toward northeast into the PNJ. Therefore, the majority of phase lines of the simulated

waves are horizontally inclined in the direction where the horizontal wind maximizes (Fig. 4).

By assuming that vertical profiles of the zonal and meridional winds $u(z)$ and $v(z)$ and the thermal stability $N(z)$ are steady in a certain period of time and have negligible horizontal gradients, the intrinsic frequency of the mountain waves can be calculated as $\hat{\omega} = -ku - lv$, where (k, l) are the components of stationary horizontal wave vector $\mathbf{k}_H$. For the dominating westerlies, v is omitted and $k = 2\pi/\lambda_x$. Using typical zonal mountain ridge extensions $\lambda_x \approx 10, \ldots,$ 100 km and zonal winds at 700 hPa ranging from 10 to 20 m s^{-1}, $|\hat{\omega}| \approx 6, \ldots, 120f$, with $f = 10^{-4}$ s^{-1}. This means most of the excited waves are medium- to high-frequency waves according to the terminology of Fritts and Alexander (2003). Indeed, the maximum estimated intrinsic frequency $\hat{\omega} \approx 0.0125$ s^{-1} is close to the tropospheric value of the buoyancy frequency N. It is known from linear theory that the associated short- and high-frequency waves can be partially reflected by the increasing wind in the stratosphere (Schoeberl 1985). Another possibility is the tunneling of high-frequency modes through the PNJ, an essentially nonhydrostatic process not represented in ERA5 (Mixa et al. 2021). Therefore, only the horizontally longer, medium- to long-frequency waves are found in the numerical simulation results. Linear wave theory can also be used to compare the simulated values of the vertical wavelength λ_z with estimates by the approximated, linear dispersion relation $m^2 = N^2/u^2$. Using stratospheric values at the equatorward edge of the PNJ of $N = 0.02$ s^{-1} and $u \approx 60, \ldots, 80$ m s^{-1}, $\lambda_z = 2\pi/|m| \approx 18, \ldots, 25$ km. Comparing to the aforementioned findings of $\lambda_z \approx 18 \pm 2$ km based on Fig. 14a, the lower value of the linear estimate corresponds to the equatorward edge of the PNJ. Larger horizontal winds cause an increase of λ_z. Thus, the agreement between the estimates based on linear mountain wave theory and the results of the numerical simulations underpins the findings so far.

d. *Wave energy fluxes*

Further evidence is provided by Fig. 18 displaying the vertical energy flux $EF_z = w'p'$ at three stratospheric pressure levels. In the lower stratosphere at 100 hPa, positive energy fluxes $EF_z \approx 3$ W m^{-2} are found in the vicinity of the major European mountain ranges: in the lee of the Pyrenees, over the Alps, the Apennines, the Dinaric Alps, and the Caucasus. Already at 10 hPa (about 30 km altitude) the positive energy fluxes $EF_z \approx 1$ W m^{-2} spread horizontally over Middle and Eastern Europe into the northeastern direction. Figure 18a reveals two interesting processes. First, the bow-shaped patterns at around 10°E point to horizontally spreading mountain waves. Second, the patches with positive EF_z between 25° and 50°E are signatures (the upper-level branches) of the obliquely propagating mountain waves (cf. Figs. 13a and 14b).

Figure 19 complements the horizontal sections by displaying the temporal evolution of the area-averaged vertical energy fluxes EF_z at 700 hPa and at those stratospheric levels as shown in the previous Fig. 18. At 700 hPa, there is a sequence of peaks

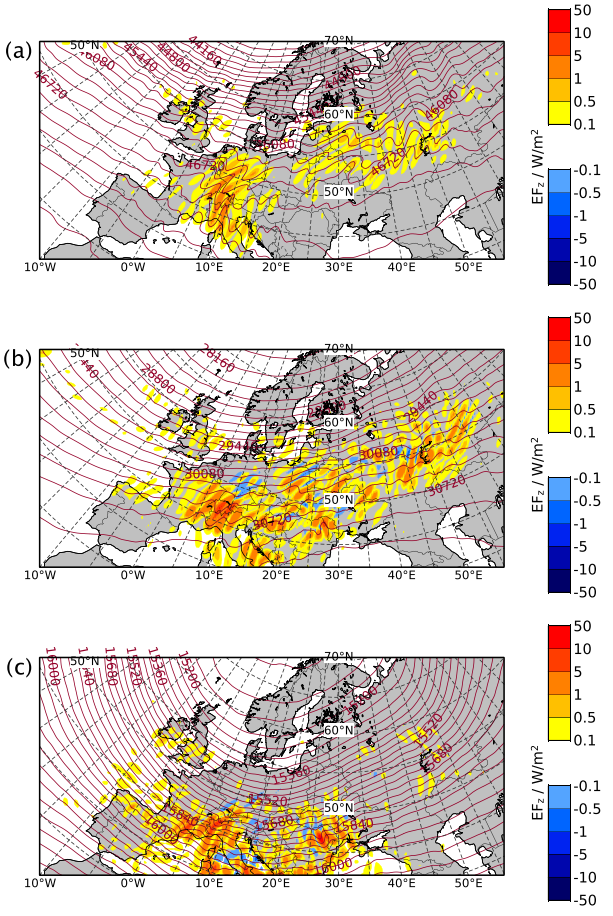

FIG. 18. Vertical energy flux EF_z (W m^{-1}, color shaded) and geopotential height (m; solid lines) at (a) 1, (b) 10, and (c) 100 hPa at 1200 UTC 12 Jan 2016.

in $EF_z > 2$ W m^{-2} that is related to the strong low-level winds over the individual mountain ranges: first the Pyrenees, second, the Alps, the Apennines, the Dinaric Alps, and, finally, the Carpathians (see section 3a). The other control areas (Middle European mountain ranges, Scandinavia, and Russia) have very small EF_z values less than 1 W m^{-2} (Fig. 19d). At 100 hPa, a similar temporal evolution of EF_z for all control areas is found; however, the magnitude of EF_z is reduced but peaks of $EF_z > 1$ W m^{-2} are attained over the Pyrenees, the Alps, the Apennines, and the Dinaric Alps (Fig. 19c).

The temporal sequences change drastically in the upper stratosphere at 10 and 1 hPa (Figs. 19a,b). Over the Pyrenees, EF_z attenuates between 10 and 1 hPa and the mountain waves cannot penetrate higher up, cf. horizontal sections in Fig. 13. In contrast, the larger EF_z values of about 0.6, ..., 1.6 W m^{-2} over the Alps indicate a deep vertical propagation that is related to the enhanced wind of the PNJ at this latitude. Interestingly, the EF_z values over Middle Europe and over Russia increase in magnitudes. This particular finding indicates that wave energy is propagated obliquely into these distant areas implying an impact on the ambient winds (see section 5). At the highest pressure level, the EF_z values of

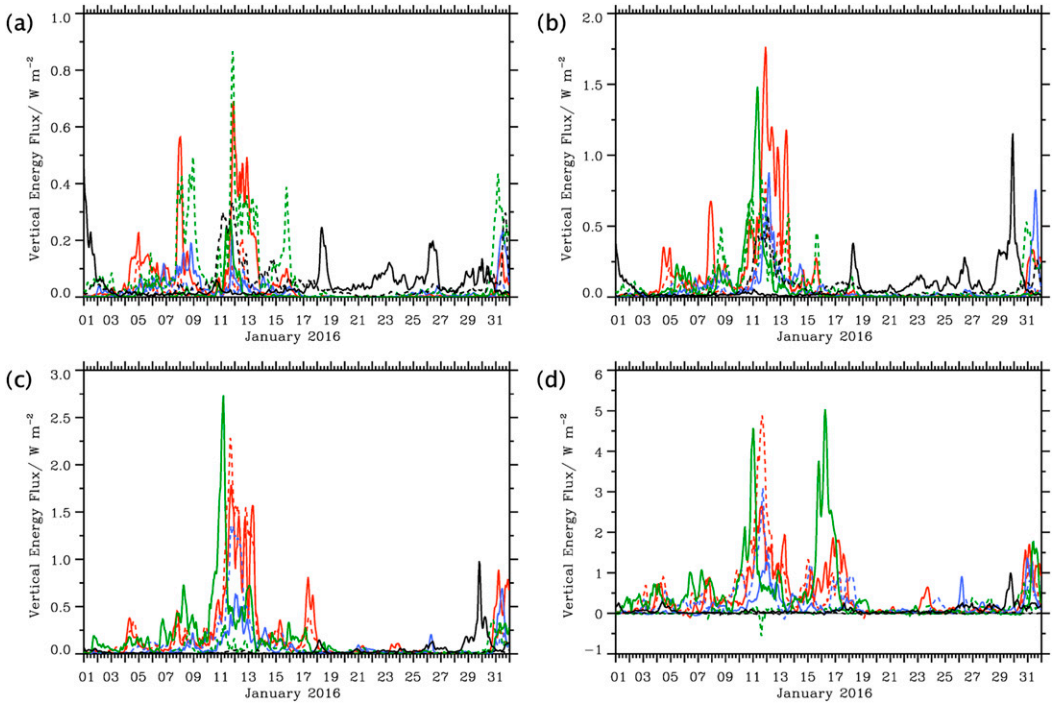

FIG. 19. Temporal evolution of the vertical energy flux EF_z at (a) 1, (b) 10, (c) 100, and (d) 700 hPa as area averages for the eight control areas. The line style is the same as used for plotting their circumferences in Fig. 6.

nearly 1 W m^{-2} over Middle Europe even surpass all other area averages.

Further evidence for the stratospheric gravity waves originating from the flow across the mountains is provided by the temporal course of the area-averaged zonal energy fluxes $EF_x = \overline{u'p'}$ at the upper stratospheric levels 1 and 10 hPa in Figs. 20a and 20b. As expected for mountain waves, energy is transported against the mean westerly flow, and therefore, EF_x is negative in all control areas. The largest magnitudes of EF_x are calculated for the Alps, and the Pyrenees at 10 hPa. Interestingly, at 1 hPa $|EF_x|$ maximizes over the Alps, the Middle European mountain ranges, and Russia. The occurrence of these peaks over areas far north of the wave source is a strong indication that the analyzed stratospheric gravity waves are mountain waves. Figures 20c and 20d display meridional energy flux EF_y and, again, the largest values at 1 hPa are calculated for both northern areas. The large meridional gradients of the zonal wind with latitude leads to a poleward advection of wave energy away from the mountain sources, i.e., $EF_y > 0$.

Recently, Jiang et al. (2019) investigated similar wave modes shed from the flow over New Zealand during the Deep Propagating Gravity Wave Experiment (DEEPWAVE) campaign (Fritts et al. 2016) and termed them trailing waves. Their horizontal focusing into the PNJ is the same as the ones analyzed here by the ERA5 data and shown in Fig. 13. Therefore, they are named: stratospheric mountain waves trailing across Northern Europe. Earlier work on the focusing and refraction of internal gravity waves were provided by Dunkerton (1984), Preusse et al. (2002), and Sato et al. (2012). Other recent examples of oblique wave propagation were given among others by Ehard et al. (2017) and Gupta et al. (2021).

e. Comparison to other episodes

In this subsection, the question ''How do the mountain wave amplitudes or energy fluxes found during this mountain event work compare with the results of previous field campaigns dealing with stratospheric gravity waves?'' is answered. Four stratospheric gravity wave campaigns are selected: T-REX (Grubišić et al. 2008), DEEPWAVE (Fritts et al. 2016), Gravity Wave Life Cycle (GWLCYCLE) (Wagner et al. 2017), and Southern Hemisphere Transport, Dynamics, and Chemistry–Gravity Waves (SOUTHTRAC-GW) (Rapp et al. 2021). The period covered in this paper belongs to GWLCYCLE. For each of the campaigns, two complete months are specified: March and April 2006 for T-REX, June and July 2014 for DEEPWAVE, December 2015 and January 2016 for GWLCYCLE, and August and September 2019 for SOUTHTRAC-GW, respectively. Variances, energy, and momentum fluxes as well as the horizontal wind components are analyzed by means of hourly ERA5 data averaged at each time in areas covering mountain ranges probed by the individual campaigns. The T-REX area encloses the Sierra Nevada in a box with the S–W–N–E coordinates of 35°–38°N, 120°–116°W, the DEEPWAVE area encloses the Southern Alps with the box coordinates of 47°–40°S, 165°–175°E, and for GWLCYCLE, the control areas Pyrenees, Alps, and Apennines are analyzed (see Fig. 6). For SOUTHTRAC-GW, three adjacent areas cover the southernmost part of the Andes with the coordinates of 48°–43°S,

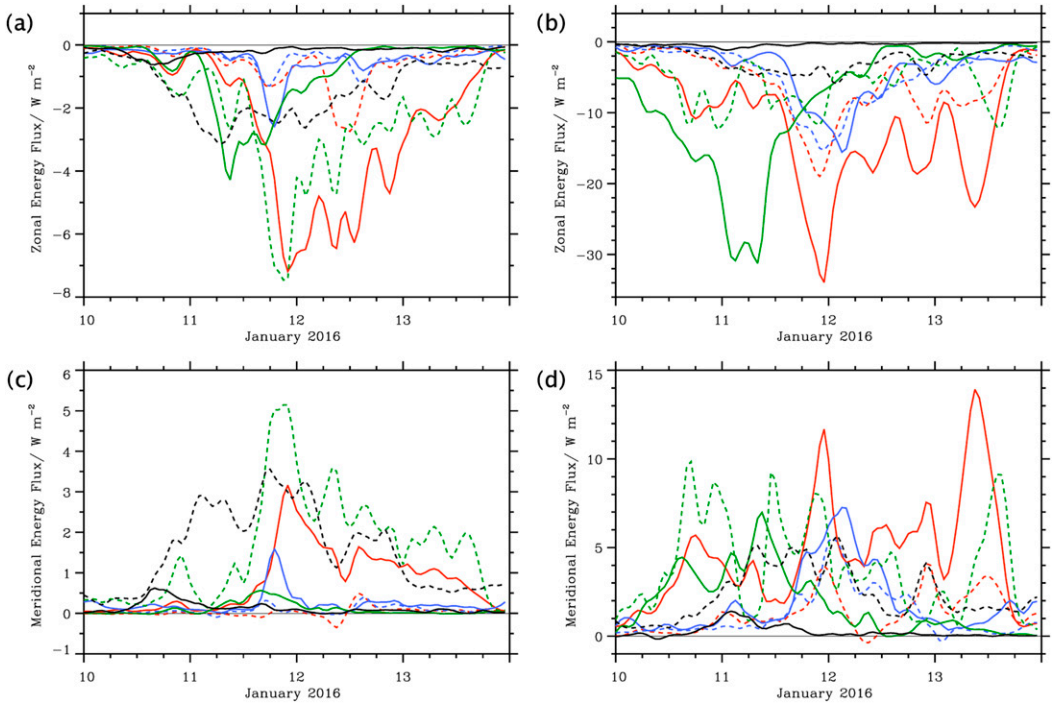

FIG. 20. Temporal evolution of the (a),(b) zonal and (c),(d) meridional energy fluxes (EF_x and EF_y, respectively) at (a),(c) 1 and (b),(d) 10 hPa as area averages for the eight control areas. The line style is the same as used for plotting their circumferences in Fig. 6.

74°–66°W; 52°–48°S, 75°–67°W; and 56°–53°S, 72°–65°W, respectively.

The probability density functions for area-averaged quantities standard deviation $\sigma_T = \sqrt{\overline{T'^2}}$, EF_z, and u at the pressure levels of 1, 10, and 300 hPa are selected and depicted in Fig. 21. At 1 hPa, the σ_T distribution peaks at small values less than 1 K for all campaign periods. Values greater than 5 K are only attained for the SOUTHTRAC-GW and the GWLCYCLE periods. The distribution for EF_z at 1 hPa peaks rather sharply at small positive values of about 0.2 W m^{-2}. Similar to σ_T, large values ($EF_z \approx 1$ W m^{-2}) are only attained for SOUTHTRAC-GW and GWLCYCLE. In this way, both periods differ from DEEPWAVE where only a few events showed large upper stratospheric amplitudes over the Southern Alps (see Bramberger et al. 2017; Ehard et al. 2017). During T-REX, deep vertical propagation was not expected and observed (Smith et al. 2008). Toward lower pressure levels, all σ_T distributions become more alike and values are limited to $\sigma_T < 2$ K in the upper troposphere (Fig. 21c). A similar convergence of the EF_z distributions is also found for the four campaigns. However, the EF_z distributions become broader and large values $EF_z > 5$ W m^{-2} are calculated at 300 hPa (Fig. 21f).

To explain these findings, probability density functions of the area-averaged zonal wind component u are added in Figs. 21g–i. Although the upper tropospheric winds at 300 hPa during all the four periods show similar, nearly Gaussian distributions with peak values between 10 and 20 m s^{-1}, the distributions differ markedly at stratospheric levels. This means that the excitation and propagation through the troposphere and lower stratosphere resemble each other during the four different campaigns. However, it is the wind at about 10 hPa allowing the mountain waves to penetrate to higher levels or filtering them out (Kruse et al. 2016). This is clearly visible for the zonal wind at 10 hPa where the u distributions for GWLCYCLE and SOUTHTRAC-GW show maxima at larger zonal winds. In this way, the considered period of this paper has smaller mountain-wave induced σ_T and EF_z extrema but compares fairly well with the values in the selected SOUTHTRAC-GW months.

5. Stratospheric wave drag

In the previous sections, the meridional propagation of mountain waves excited by the strong westerly flow across the Central European mountain ranges and moving northeastward from was described, quantified, and compared with ERA5 results from periods of previous observing campaigns. Here, the unique capability of the high-resolution ERA5 dataset is used to evaluate the contributions of resolved and parameterized stratospheric wave drag to the deceleration of the zonal mean flow. For this purpose, the resolved vertical flux of zonal momentum

$$MF_x = \rho \overline{u'w'} \tag{2}$$

is computed locally whereby—as before—the primed quantities denote deviations of the fully resolved quantities from their spectrally truncated values for horizontal wavenumbers

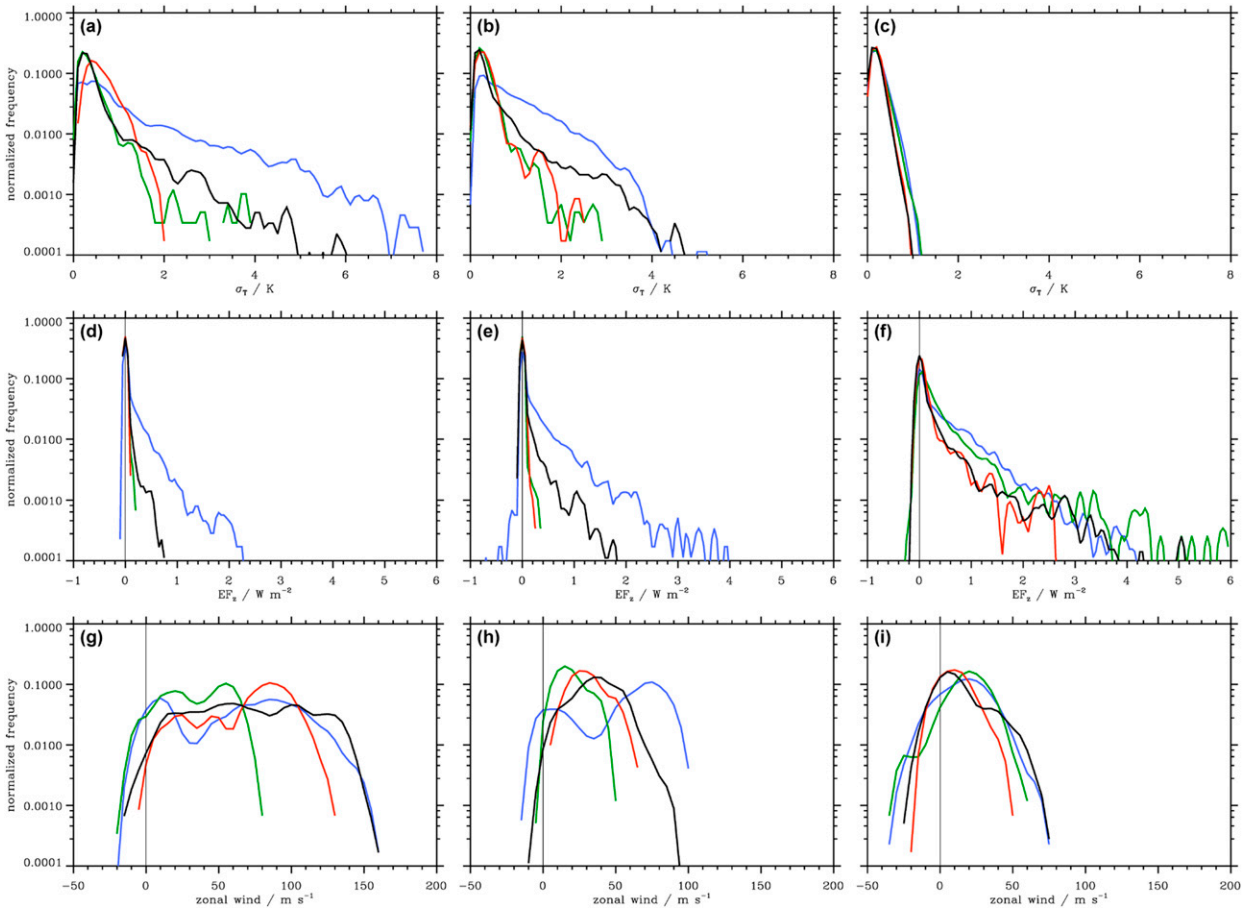

FIG. 21. Probability density functions of the area-averaged standard deviation (a)–(c) σ_T, (d)–(f) EF_z, and (g)–(i) the zonal wind u at (a),(d),(g) 1, (b),(e),(h) 10, and (c),(f),(i) 300 hPa. The different line colors denote the control areas for the campaign periods of GWLCYCLE (black), SOUTHTRAC-GW (blue), T-REX (green), and DEEPWAVE (red), see text.

less than 106 (see section 4a). The vertical momentum flux convergence is calculated by

$$\mathrm{VMFC}_x = -\frac{\partial}{\partial p}\overline{u'\omega'} \tag{3}$$

and determines the acceleration/deceleration of the mean flow by momentum deposition of the resolved gravity waves. In addition, the parameterized tendencies $\partial u/\partial t$ for the considered period 10–13 January 2016 are evaluated and compared to monthly mean values of winter 2015/16. Both VMFC_x and $\partial u/\partial t$ together represent the net forcing of the mean flow due to momentum deposition of resolved and parameterized gravity waves. All quantities are retrieved at 60 stratospheric model levels from 100 to 0.01 hPa, whereby the spacing increases from 250 m in the lower stratosphere to about 1500 m above 1 hPa. Six-hourly ERA5 analyses are used to calculate MF_x and VMFC_x. ERA5 short-term forecasts at lead times +6 and +12 h initialized at 0600 and 1800 UTC, respectively, are used to obtain the parameterized tendencies $\partial u/\partial t$.

Figure 22 compares the altitude–latitude sections of zonal means of MF_x, VMFC_x, and the parameterized tendencies $\partial u/\partial t$ for the period 10–13 January 2016, and for the January 2016 monthly means. Positive momentum $\rho u'$ is transported downward by the gravity waves, i.e., $\mathrm{MF}_x < 0$ (see Figs. 22a,b). The zonal means of MF_x are tilted into the PNJ from the source regions that are located between 40° and 50°N. In particular, for the period 10–13 January 2016, there are two branches of negative MF_x extending vertically upward. The MF_x magnitude decreases vertically and absolute values greater than 1 mPa are located only at the bottom of the stratospheric layer, as shown in Figs. 22a and 22b (see Table 1). A very similar vertical and meridional distribution is obtained for $\mathrm{MF}_y = \rho\overline{v'w'}$; however, MF_y is mostly positive implying a downward transport of negative momentum $\rho v'$ (not shown).

Vertical momentum flux convergence VMFC_x includes the net forcing of the zonal flow due to resolved gravity waves. Negative zonal-mean VMFC_x maximizes at the equatorial edge of PNJ south of 60°N at about 1 hPa for 10–13 January 2016 (Fig. 22c). Here, the vertical and meridional VMFC_x distribution extends downward toward the source region of the mountain waves in accordance with the two branches of MF_x as shown in Fig. 22a. However, VMFC_x in these branches is rather small indicating that the main deceleration occurs at about 1 hPa. The vertical increase in VMFC_x magnitude is also evident in the January 2016 monthly

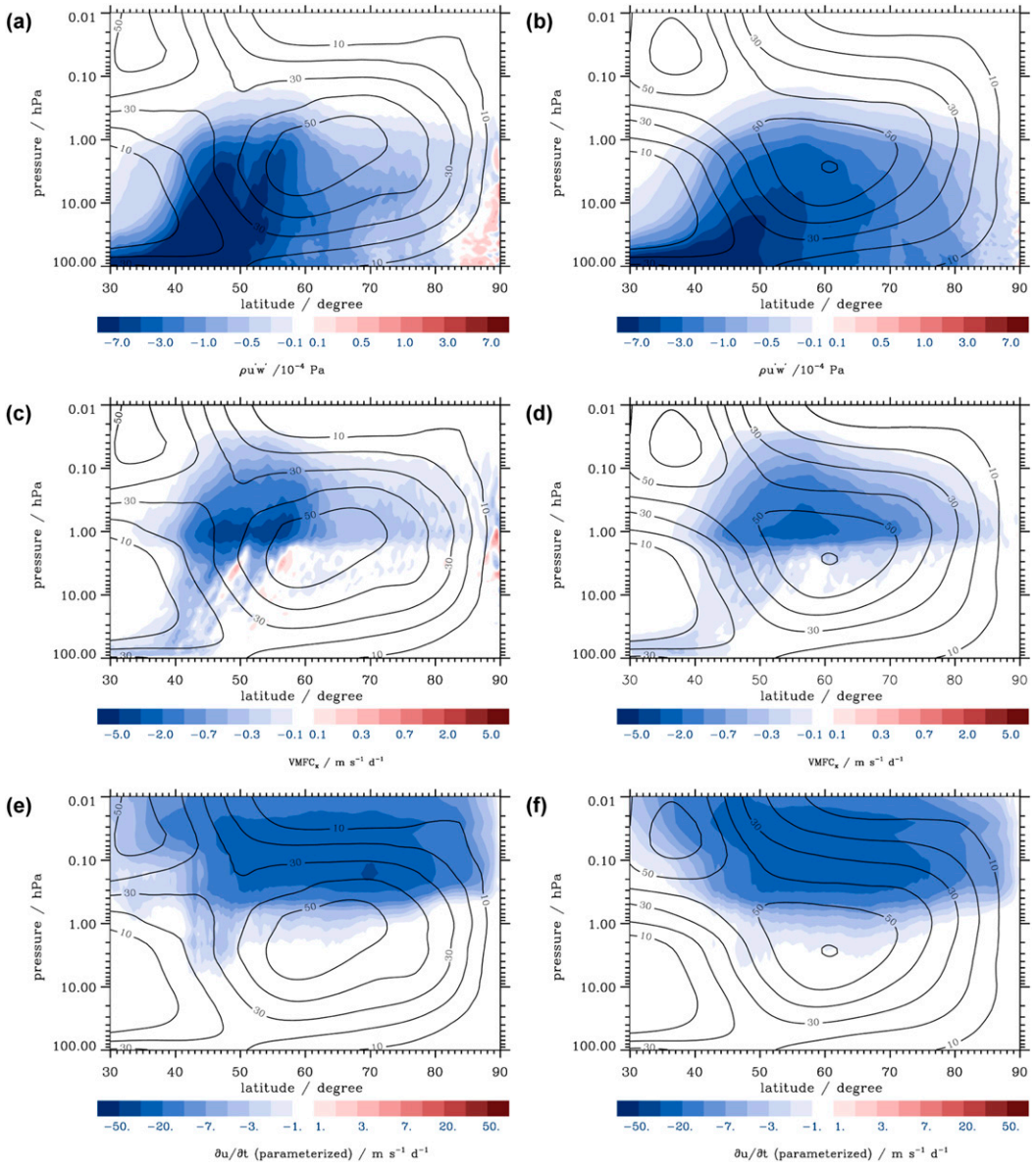

FIG. 22. Zonal-mean (top) vertical momentum flux MF_x (Pa, color shading), (middle) vertical momentum flux convergence $VMFC_x$ (m s^{-1} day^{-1}, color shading), and (bottom) parameterized tendency $\partial u/\partial t$ (m s^{-1} day^{-1}, color shading). (left) Temporal average from 10 to 13 Jan 2016. (right) Monthly means of January 2016. The black contour lines denote the zonal-mean zonal wind averaged over the respective time periods.

means, which peak here within the core of the PNJ (see Fig. 22d). The vertical position of the zonal mean $VMFC_x$ minimum of about $-3\,\mathrm{m\,s^{-1}\,day^{-1}}$ is almost unchanged during the evaluated winter months December 2015 to February 2016. Also, their peak values differ by only about 22% from November 2015 to January 2016 but drop in February 2016 (see Table 1).

The vertical decay of $VMFC_x$ at $p < 1$ hPa shows the dominant influence of the deceleration of the zonal mean flow in the sponge layer. This effect is represented by the parameterized wave drag $\partial u/\partial t$ as shown in Figs. 22e and 22f. The $\partial u/\partial t$ magnitude maximizes at levels less than 1 hPa and is broadly distributed over almost all latitudes poleward of about 40°N. In particular, over 10–13 January 2016, $\partial u/\partial t$ also extends downward, similar to $VMFC_x$ (cf. Figs. 22c,e). Inside the PNJ, values peak at about $-30\,\mathrm{m\,s^{-1}\,day^{-1}}$ for January 2016. From December 2015 to February 2016, the magnitude of the maximum $\partial u/\partial t$ values decreases in line with the subsiding zonal wind within the PNJ (see Table 1). Since $\partial u/\partial t$ represents the parameterized wave drag by orographic as well as by nonorographic gravity waves, this result implies that less large-amplitude parameterized gravity waves contribute to the wave drag because they are filtered out and cannot penetrate to higher levels. Zonal means of the parameterized tendencies $\partial u/\partial t$ are negligible in comparison to $\partial u/\partial t$ (not shown).

TABLE 1. Peak values of the monthly mean zonally averaged zonal wind u, vertical flux of zonal momentum MF_x, the vertical momentum flux convergence $VMFC_x$, and the parameterized wave drag $\partial u/\partial t$ at levels higher than 100 hPa.

Period	u (m s^{-1})	MF_x (mPa)	$VMFC_x$ (m s^{-1} day^{-1})	$\partial u/\partial t$ (m s^{-1} day^{-1})
Nov 2015	68.0	−1.27	−2.6	−48.8
Dec 2015	85.6	−1.76	−3.3	−44.1
Jan 2016	65.5	−2.12	−2.9	−29.5
Feb 2016	54.3	−1.94	−2.4	−14.9
10–13 Jan 2016	57.9	−3.79	−4.5	−32.2

The hemispherical distributions for the three quantities at about 1 hPa and averaged over the two time periods are juxtaposed in Fig. 23. An elongated band of large negative MF_x and $VMFC_x$ is clearly detectable over Central Europe extending into the eastern part of Russia. It is located at the equatorial edge of the PNJ (see Figs. 23a,b). Local MF_x and $VMFC_x$ values peak at −14.1 mPa and −208 m s^{-1} day^{-1} in the period 10–13 January 2016 (see Table 2). The peak January 2016 monthly means are smaller: −2.81 mPa and −30.8 m s^{-1} day^{-1} (see Table 3). Estimates of total momentum flux $MF = \sqrt{MF_x^2 + MF_y^2}$ and $VMFC_x$ for a large-amplitude mountain wave event, observed in the lee of the Andes, yielded mean values of about 10, . . . , 20 mPa and −50 m s^{-1} day^{-1} at around 50-km altitude (Kaifler et al. 2020, Figs. 2d and 2c). Moreover, the altitude dependence of the absolute values of MF_x and $VMFC_x$ (Tables 2 and 3) is similar to the results reported by Kaifler et al. (2020). These numbers, along with estimates by Gupta et al. (2021) discussing a different

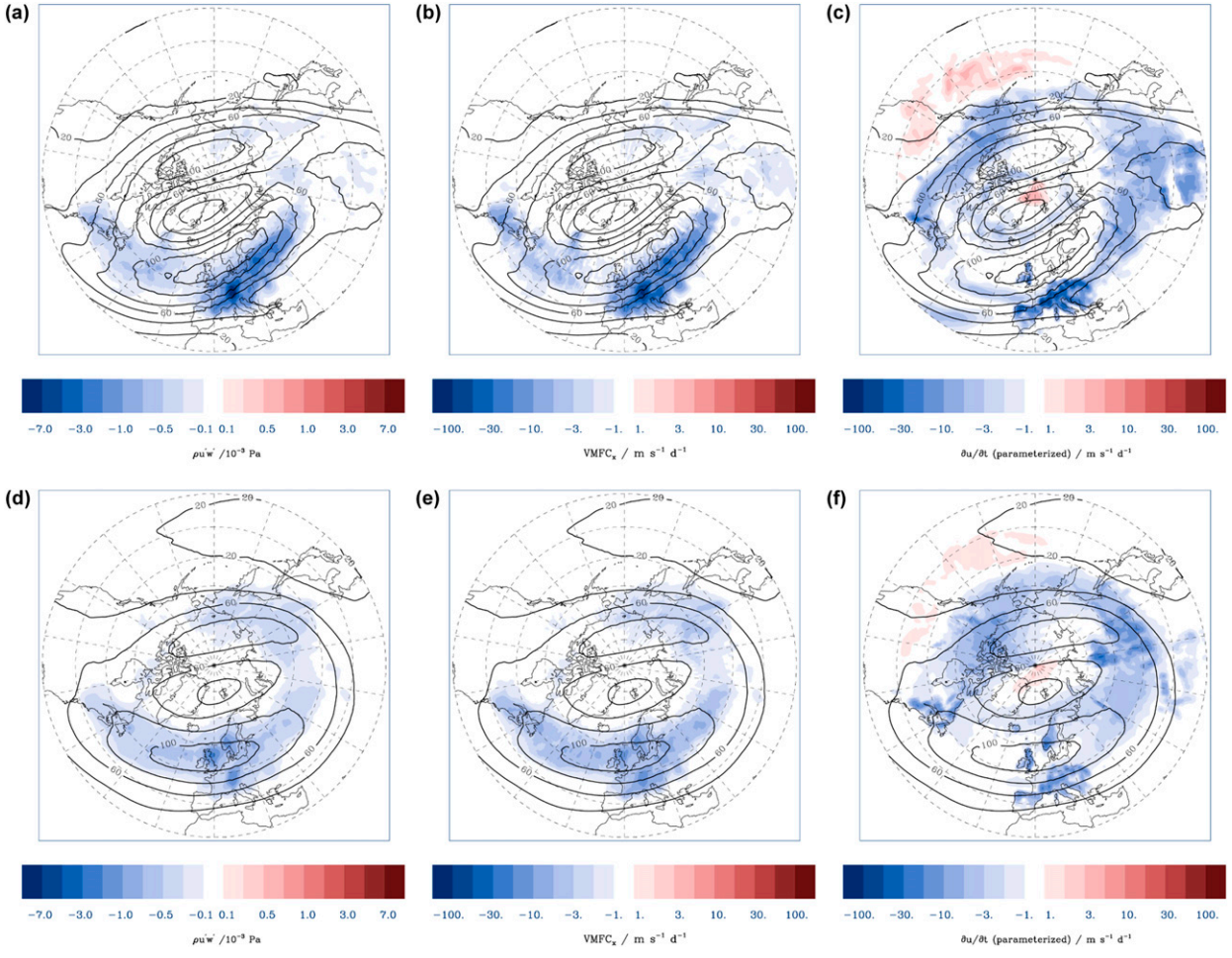

FIG. 23. (left) Vertical momentum flux MF_x (Pa, color shading), (center) vertical momentum flux convergence $VMFC_x$ (m s^{-1} day^{-1}, color shading), and (right) parameterized tendency $\partial u/\partial t$ (m s^{-1} day^{-1}, color shading). The values are vertical averages over four model levels around 1 hPa. (top) Temporal average from 10 to 13 Jan 2016. (bottom) Monthly means of January 2016. The black contour lines denote the zonal wind averaged over the respective time periods.

TABLE 2. Peak values of the mean zonal wind u, vertical flux of zonal momentum MF_x, the vertical momentum flux convergence $VMFC_x$, and the parameterized wave drag $\partial u/\partial t$ for selected stratospheric levels in the period from 10 to 13 Jan 2016. The values are vertical averages over four to five adjacent model levels around the given pressure.

Level (hPa)	u (m s^{-1})	MF_x (mPa)	$VMFC_x$ (m s^{-1} day^{-1})	$\partial u/\partial t$ (m s^{-1} day^{-1})
0.1	92.5	−0.17	−30.3	−499.6
1.0	129.3	−14.10	−208.0	−291.1
10.0	109.5	−53.08	−39.9	−80.1
50.0	50.6	−136.06	−45.0	−50.3

mountain wave event over the Andes (their Fig. 1), lead to the conclusion that the deceleration of the mean flow by gravity waves excited by the flow over the Alps reaches magnitudes similar to the Southern Hemispheric large-amplitude mountain wave events.

The parameterized wave drag is also large over the Central European mountains, as shown in Figs. 23c and 23f. Moreover, large $\partial u/\partial t$ values are widely distributed within the Arctic polar vortex, and elevated levels at different locations indicate different sources, whether orographic or nonorographic ones. Tables 2 and 3 show that the weakening of the zonal flow by $\partial u/\partial t$ increases by a factor of 100 from 50 Pa to 0.01 hPa, while the monthly mean values for $VMFC_x$ in the stratosphere have the same order of magnitude (cf. Table 3). Furthermore, the convergence of the mountain waves into the PNJ resembles the situation in the austral winter stratosphere where mountain waves from the Andes and the Antarctic peninsula focus into the Antarctic polar vortex (e.g., Preusse et al. 2002; Sato et al. 2012). The January 2016 hemispheric distribution of monthly means of MF_x, $VMFC_x$, and $\partial u/\partial t$ shown in Fig. 23 is similar to the gravity wave belt regularly detected in the Southern Hemisphere (Hendricks et al. 2014). However, here the Arctic polar vortex was disturbed by planetary waves in January 2016 (see section 2b and appendix) and the distributions are not as zonally symmetric as their Southern Hemispheric counterparts. However, the monthly means still show extreme values over Europe. Yet their magnitudes are smaller than the values for 10–13 January 2016 but underscore the significant contribution of the 4-day mountain wave event to the monthly means.

Finally, the question of how much a single mountain wave event such as the one considered in the paper contributes to the overall deceleration of the zonal wind in the polar vortex is addressed. Therefore, a cumulative zonal wind increment

$$\Delta u(t^n) = \int_{t^0}^{t^n} f(t)dt \qquad (4)$$

is calculated for all previously defined control areas that are sketched in Fig. 6. In Eq. (4), $f(t)$ stands either for 6-hourly $VMFC_x$ or for 6-hourly $\partial u/\partial t$ as described above. The functions $f(t)$ are calculated at 1 hPa and are integrated starting at $t^0 = 0$ (0000 UTC 1 January 2016) with an increment of $dt = 6$ h. Figure 24 shows the temporal evolution of $VMFC_x$ and $\partial u/\partial t$ as well as Δu due to resolved and parameterized gravity waves. The mountain wave event is reflected in an increase in both $VMFC_x$ and $\partial u/\partial t$ magnitudes for all selected control areas around 12 January 2016 (see Figs. 24a,b). The largest magnitudes of about -100 m s^{-1} day^{-1} (for $VMFC_x$) and -70 m s^{-1} day^{-1} (for $\partial u/\partial t$) are reached for the control areas encompassing significant orography (Alps, Pyrenees, mid-Europe) but also the control area Russia shows a comparable increase during this period. As mentioned earlier, the rise in successive control areas (from west to east) is temporally staggered due to the changing forcing conditions (see section 3a).

In contrast to the large values in the regional domains, zonally averaged values of $VMFC_x$ and $\partial u/\partial t$ show only a marginal increase of less than -5 m s^{-1} day^{-1} in this period (gray lines in Figs. 24a,b).

Consequently, the values of Δu increase drastically during the mountain wave event 10–13 January 2016 and achieve local values of -200 m s^{-1} for the resolved and for the parameterized gravity waves. However, they occur quite regionally over a relatively short period of time. It is obvious that such regional deceleration cannot last long. And the final net deceleration of the horizontal wind V_H of about 40 m s^{-1} day^{-1}, as estimated earlier in relation to Fig. 17c, also suggest that terms other than $VMFC_x$ and the parameterized wave drag determine the net momentum budget. After the mountain wave event, the horizontal progression of the Δu curves over the mountains indicates that no gravity waves are excited from the respective control regions and propagate upward. A comparison with Fig. 3c of Gupta et al. (2021) reveals that the regional cumulative zonal wind increments Δu are indeed extremely large. To relate their results to these Northern Hemispheric values,

TABLE 3. Peak values of the monthly mean zonal wind u, vertical flux of zonal momentum MF_x, the vertical momentum flux convergence $VMFC_x$, and the parameterized wave drag $\partial u/\partial t$ at selected stratospheric levels for January 2016. The values are vertical averages over four to five adjacent model levels around the given pressure.

Level (hPa)	u (m s^{-1})	MF_x (mPa)	$VMFC_x$ (m s^{-1} day^{-1})	$\partial u/\partial t$ (m s^{-1} day^{-1})
0.1	83.5	−0.09	−12.9	−248.3
1.0	110.3	−2.81	−30.8	−77.9
10.0	83.9	−8.51	−7.9	−23.8
50.0	43.2	−34.26	−10.3	−21.8

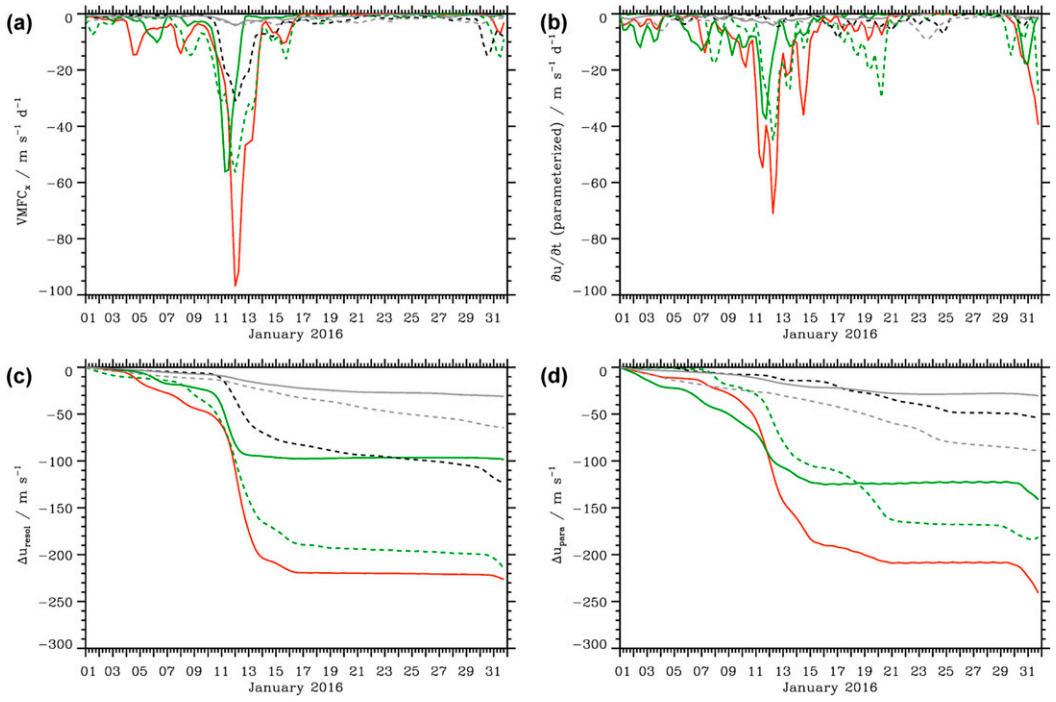

FIG. 24. Temporal evolution of (a) area-averaged vertical zonal momentum flux convergence $VMFC_x$ and (b) the parameterized tendency $\partial u/\partial t$ at 1 hPa. (c),(d) The cumulative zonal velocity increments Δu due to the deceleration by (c) resolved and (d) parameterized gravity waves. The line style is the same as used for plotting their circumferences in Fig. 6—solid red: Alps; solid green: Pyrenees, dashed green: Middle European mountain ranges; dashed black: Russia. The solid and dashed gray lines denote zonal means in latitude bands from 40° to 50°N and from 50° to 60°N, respectively. Data: ERA5.

Figs. 24c and 24d also show zonal means in two latitude bands (solid and dashed gray lines). The temporal evolution of these values corresponds to the results shown by Gupta et al. (2021). Interestingly, the increase in Δu is larger in the northern (50°–60°N) band than in the band 40°–50°N, where the mountain wave sources are located. Furthermore, in contrast to the local control areas, zonal-mean Δu is steadily decreasing due to effects of gravity waves originating from different sources and propagating into the PNJ. This result emphasizes once again the importance of the meridional propagation of gravity waves into the PNJ. The results in Fig. 24 are only shown for the 1 hPa level; a different partition of resolved and parameterized contributions can be expected due to their different altitude distributions (see Fig. 22 and Tables 2 and 3).

6. Summary and conclusions

The attempt of the paper to document the stratospheric waves during a particularly interesting period in the middle of January 2016 in which the Arctic polar vortex was displaced by planetary wave activity was achieved by analyzing the ERA5 data. The synoptic situation was dominated by a strong low-level flow across all European mountain ranges and an upper-level trough that expanded south. The associated polar-front jet was nearly aligned with the polar night jet. These circumstances led to favorable conditions for mountain wave excitation and meridional propagation. Three major findings support the hypothesis that the analyzed waves are mountain waves: (i) The quasi stationarity of the phase fronts during certain periods and their vertical inclination against the westerly winds while propagating from the troposphere to the stratosphere and (ii) the positive vertical and the negative zonal and meridional energy fluxes found above the major European mountain ranges. Eventually, (iii) the estimated intrinsic frequencies were below the Coriolis parameter and rarely attained values larger than the buoyancy frequency. The deep vertical and meridional propagation of the mountain waves was unique due to a poleward shift of the upper portion of the Arctic polar vortex. The planetary wave disturbance of the polar vortex resulted in a flow configuration enabling the mountain waves trailing into the stratosphere across Northern Europe as analyzed by ERA5.

In section 4e, area-averaged probability density distributions of $\sigma_T = \sqrt{\overline{T'^2}}$, EF_z, and the zonal wind u at 1, 10, and 300 hPa are presented for four periods of different airborne campaigns devoted to stratospheric gravity waves. The results at 1 hPa convincingly show that maximum values of $\sigma_T \approx 5$ K and $EF_z \approx 1\,W\,m^{-2}$ during the considered period of January 2016 belong to large-amplitude mountain wave events that were also found during August and September 2019 over the southern Andes during SOUTHTRAC-GW. In contrast, due to stratospheric wind filtering, both the T-REX as well as the

DEEPWAVE campaigns have much smaller upper-stratospheric mountain wave amplitudes despite similar excitation and tropospheric propagation conditions.

Criteria commonly used to identify regions of spontaneous emission of nonorographic gravity waves or inertially unstable regions indicate that these processes are unlikely. Furthermore, one should admit that the large-amplitude mountain waves trailing across the European continent were not present in the ERA5 data before the tropospheric weather system made landfall. Finally, there are also no indication of large-amplitude T' perturbations in the PNJ upstream over the northern Atlantic.

The unique capability of ERA5 allows the determination of the wave drag due to resolved as well as parameterized gravity waves. Here, zonal-mean peak values of -4.5 and $-32.2\,\mathrm{m\,s^{-1}\,day^{-1}}$ were calculated for VMFC_x and $\partial u/\partial t$ at 1 hPa during the mountain wave period 10–13 January 2016. The evaluated magnitudes of zonal means of VMFC_x, and $\partial u/\partial t$ are only slightly larger and represent a physically reasonable spatial distribution. The especially large magnitudes that were achieved during the mountain wave period indicate the substantial impact of regional and remote gravity wave forcing onto the PNJ. The substantial deceleration of the zonal mean flow by resolved and parameterized gravity thus suggests its important contribution during vortex decay, a question systematically addressed by Gupta et al. (2021).

Quantifying the wave properties of such an extended stratospheric wave field with observations, e.g., airborne remote sensing instruments such as a Rayleigh lidar is challenging for several reasons. To cover the whole wave fields, research flights tracks should be kept as simple, straight, and long as possible. It could be desirable to align the flight tracks with the mean wind at flight level. This approach at least facilitates the exact determination of momentum and energy fluxes at flight levels (Smith et al. 2008, 2016). The change of the phase lines of mountain waves with altitude constitutes a difficult task for exactly estimating the horizontal wavelength in cases the legs are not parallel to the wave vector. This problem of the analysis could be solved experimentally by simultaneous airborne observations with a fleet of research aircraft operating at horizontally staggered parallel legs. As this approach is hardly feasible it might help to identify dominant wave modes using reliable three-dimensional meteorological data from state-of-the art NWP models. The finer resolution and increasing realism of model outputs like the ones used in this study offers a valuable quantitative source for mesoscale flow components that were hitherto not accessible globally (Bauer et al. 2015). Even higher resolved numerical models might open views beyond the presented findings and might allow for modified conclusions.

Acknowledgments. This research was partly funded by the Deutsche Forschungsgemeinschaft (DFG) via the project MS-GWaves (GW-TP/DO 1020/9-1, PACOG/RA 1400/6-1) and by the German research initiative "Role of the middle atmosphere in climate" (ROMIC) under Grant 01LG1206A provided by the Federal Ministry for Education and Research. Access to ECMWF data was granted through the special project "Deep Vertical Propagation of Internal Gravity Waves."

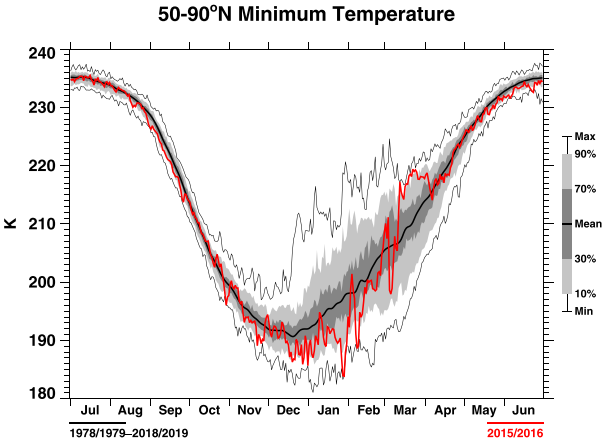

FIG. A1. Polar cap minimum temperature for the Northern Hemisphere at 30 hPa. The red curve shows the evolution for the Northern Hemispheric winter 2015/16, and the black curve the climatological mean.

Data availability statement. The ERA5 data used in this study can be retrieved from the following website: https://confluence.ecmwf.int/display/CKB/How+to+download+ERA5.

APPENDIX

Evolution of the Arctic Polar Vortex

Modern-Era Retrospective Analysis for Research and Applications, version 2 (MERRA-2), climatological data (Gelaro et al. 2017) are used to document the evolution of Arctic polar vortex in the winter 2015/16, especially, the disturbances occurring in the middle of January 2016. All plots were created using the visualization web page https://acd-ext.gsfc.nasa.gov/Data_services/met/ann_data.html. The exceptionally cold Arctic winter is proven by the plot of the polar cap minimum temperature T_{MIN} at 30 hPa in Fig. A1.

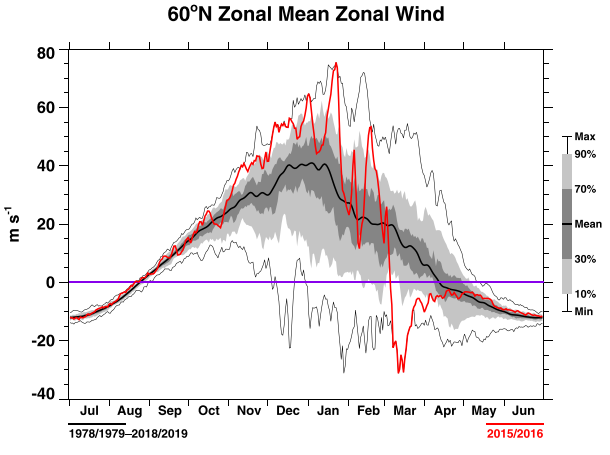

FIG. A2. zonal-mean zonal wind at 60°N at 10 hPa. The red curve shows the evolution for the Northern Hemispheric winter 2015/16, and the black curve the climatological mean.

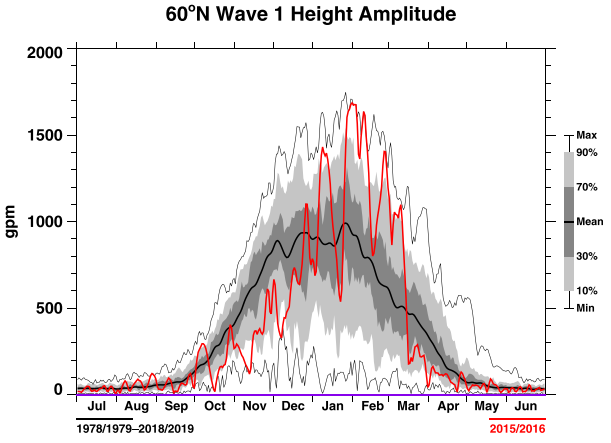

FIG. A3. Amplitude of the zonal wavenumber 1 at 60°N and 10 hPa. The red curve shows the evolution for the Northern Hemispheric winter 2015/16, and the black curve the climatological mean.

Inside the polar vortex, T_{MIN} was below the climatological mean between December 2015 and the final warming begin of March 2016. In January 2016, vortex-wide ice PSCs were found in airborne observations (Voigt et al. 2018).

Two different indicators are selected to document the disturbances of the Arctic polar vortex due to planetary waves. First, Fig. A2 displays the longitudinally averaged zonal wind U at 60°N as an indicator of the strength of the polar vortex. After a nearly even increase of U until the end of 2015 (Matthias et al. 2016), the zonal wind at 60°N is decelerated indicating the disturbance of the Arctic polar vortex at the beginning of January 2016. This disturbance is due to a shift of the polar vortex leading to enhanced amplitude to the geopotential height amplitude of zonal wavenumber 1 (see Fig. A3). A second, stronger disturbance occurred at the end of January 2016 and was the subject of the study by Dörnbrack et al. (2018).

REFERENCES

Alexander, S. P., A. R. Klekociuk, A. J. McDonald, and M. C. Pitts, 2013: Quantifying the role of orographic gravity waves on polar stratospheric cloud occurrence in the Antarctic and the Arctic. *J. Geophys. Res. Atmos.*, **118**, 11 493–11 507, https://doi.org/10.1002/2013JD020122.

Arakawa, H., 1952: Severe turbulence resulting from excessive wind-shear in tropical cyclones. *J. Meteor.*, **9**, 221–223, https://doi.org/10.1175/1520-0469(1952)009<0221:STRFEW>2.0.CO;2.

Bauer, P., A. Thorpe, and G. Brunet, 2015: The quiet revolution of numerical weather prediction. *Nature*, **525**, 47–55, https://doi.org/10.1038/nature14956.

Bossert, K., S. L. Vadas, L. Hoffmann, E. Becker, V. L. Harvey, and M. Bramberger, 2020: Observations of stratospheric gravity waves over Europe on 12 January 2016: The role of the polar night jet. *J. Geophys. Res. Atmos.*, **125**, e2020JD032893, https://doi.org/10.1029/2020JD032893.

Bramberger, M., and Coauthors, 2017: Does strong tropospheric forcing cause large-amplitude mesospheric gravity waves? A DEEPWAVE case study. *J. Geophys. Res. Atmos.*, **122**, 11 422–11 443, https://doi.org/10.1002/2017JD027371.

——, A. Dörnbrack, H. Wilms, S. Gemsa, K. Raynor, and R. Sharman, 2018: Vertically propagating mountain waves—A hazard for high-flying aircraft? *J. Appl. Meteor. Climatol.*, **57**, 1957–1975, https://doi.org/10.1175/JAMC-D-17-0340.1.

Dörnbrack, A., M. Leutbecher, J. Reichardt, A. Behrendt, K.-P. Müller, and G. Baumgarten, 2001: Relevance of mountain wave cooling for the formation of polar stratospheric clouds over Scandinavia: Mesoscale dynamics and observations for January 1997. *J. Geophys. Res.*, **106**, 1569–1581, https://doi.org/10.1029/2000JD900194.

——, M. C. Pitts, L. R. Poole, Y. J. Orsolini, K. Nishii, and H. Nakamura, 2012: The 2009–2010 Arctic stratospheric winter—General evolution, mountain waves and predictability of an operational weather forecast model. *Atmos. Chem. Phys.*, **12**, 3659–3675, https://doi.org/10.5194/acp-12-3659-2012.

——, S. Gisinger, M. C. Pitts, L. R. Poole, and M. Maturilli, 2017: Multilevel cloud structures over Svalbard. *Mon. Wea. Rev.*, **145**, 1149–1159, https://doi.org/10.1175/MWR-D-16-0214.1.

——, and Coauthors, 2018: Gravity waves excited during a minor sudden stratospheric warming. *Atmos. Chem. Phys.*, **18**, 12 915–12 931, https://doi.org/10.5194/acp-18-12915-2018.

Dunkerton, T. J., 1984: Inertia–gravity waves in the stratosphere. *J. Atmos. Sci.*, **41**, 3396–3404, https://doi.org/10.1175/1520-0469(1984)041<3396:IWITS>2.0.CO;2.

Dutton, J. A., 1976: *The Ceaseless Wind*. 1st ed. McGraw-Hill, 579 pp.

Eckermann, S. D., J. Ma, and D. Broutman, 2015: Effects of horizontal geometrical spreading on the parameterization of orographic gravity wave drag. Part I: Numerical transform solutions. *J. Atmos. Sci.*, **72**, 2330–2347, https://doi.org/10.1175/JAS-D-14-0147.1.

——, J. D. Doyle, P. A. Reinecke, C. A. Reynolds, R. B. Smith, D. C. Fritts, and A. Dörnbrack, 2019: Stratospheric gravity wave products from satellite infrared nadir radiances in the planning, execution, and validation of aircraft measurements during DEEPWAVE. *J. Appl. Meteor. Climatol.*, **58**, 2049–2075, https://doi.org/10.1175/JAMC-D-19-0015.1.

Ehard, B., and Coauthors, 2017: Horizontal propagation of large-amplitude mountain waves into the polar night jet. *J. Geophys. Res. Atmos.*, **122**, 1423–1436, https://doi.org/10.1002/2016JD025621.

——, S. Malardel, A. Dörnbrack, B. Kaifler, N. Kaifler, and N. Wedi, 2018: Comparing ECMWF high-resolution analyses with lidar temperature measurements in the middle atmosphere. *Quart. J. Roy. Meteor. Soc.*, **144**, 633–640, https://doi.org/10.1002/qj.3206.

Fritts, D. C., and M. J. Alexander, 2003: Gravity wave dynamics and effects in the middle atmosphere. *Rev. Geophys.*, **41**, 1003, https://doi.org/10.1029/2001RG000106.

——, and Coauthors, 2016: The Deep Propagating Gravity Wave Experiment (DEEPWAVE): An airborne and ground-based exploration of gravity wave propagation and effects from their sources throughout the lower and middle atmosphere. *Bull. Amer. Meteor. Soc.*, **97**, 425–453, https://doi.org/10.1175/BAMS-D-14-00269.1.

Gelaro, R., and Coauthors, 2017: The Modern-Era Retrospective Analysis for Research and Applications, version 2 (MERRA-2). *J. Climate*, **30**, 5419–5454, https://doi.org/10.1175/JCLI-D-16-0758.1.

Grubišić, V., and Coauthors, 2008: The Terrain-Induced Rotor Experiment: A field campaign overview including observational highlights. *Bull. Amer. Meteor. Soc.*, **89**, 1513–1534, https://doi.org/10.1175/2008BAMS2487.1.

Gupta, A., T. Birner, A. Dörnbrack, and I. Polichtchouk, 2021: Importance of gravity wave forcing for springtime southern polar vortex breakdown as revealed by ERA5. *Geophys. Res. Lett.*, **48**, e2021GL092762, https://doi.org/10.1029/2021GL092762.

Hendricks, E. A., J. D. Doyle, S. D. Eckermann, Q. Jiang, and P. A. Reinecke, 2014: What is the source of the stratospheric gravity wave belt in austral winter? *J. Atmos. Sci.*, **71**, 1583–1592, https://doi.org/10.1175/JAS-D-13-0332.1.

Hersbach, H., and Coauthors, 2020: The ERA5 global reanalysis. *Quart. J. Roy. Meteor. Soc.*, **146**, 1999–2049, https://doi.org/10.1002/qj.3803.

Jiang, Q., J. D. Doyle, S. D. Eckermann, and B. P. Williams, 2019: Stratospheric trailing gravity waves from New Zealand. *J. Atmos. Sci.*, **76**, 1565–1586, https://doi.org/10.1175/JAS-D-18-0290.1.

Kaifler, N., B. Kaifler, A. Dörnbrack, M. Rapp, J. L. Hormaechea, and A. de la Torre, 2020: Lidar observations of large-amplitude mountain waves in the stratosphere above Tierra del Fuego, Argentina. *Sci. Rep.*, **10**, 14529, https://doi.org/10.1038/s41598-020-71443-7.

Khaykin, S. M., A. Hauchecorne, N. Mzé, and P. Keckhut, 2015: Seasonal variation of gravity wave activity at midlatitudes from 7 years of COSMIC GPS and Rayleigh lidar temperature observations. *Geophys. Res. Lett.*, **42**, 1251–1258, https://doi.org/10.1002/2014GL062891.

Knox, J. A., 1997: Possible mechanisms of clear-air turbulence in strongly anticyclonic flows. *Mon. Wea. Rev.*, **125**, 1251–1259, https://doi.org/10.1175/1520-0493(1997)125<1251:PMOCAT>2.0.CO;2.

——, 2003: Inertial instability. *Encyclopedia of Atmospheric Sciences*, J. R. Holton, J. Pyle, and J. A. Curry, Eds., Academic Press, 1004–1013, https://doi.org/10.1016/B0-12-227090-8/00175-5.

Koch, S. E., and P. B. Dorian, 1988: A mesoscale gravity wave event observed during CCOPE. Part III: Wave environment and probable source mechanisms. *Mon. Wea. Rev.*, **116**, 2570–2592, https://doi.org/10.1175/1520-0493(1988)116<2570:AMGWEO>2.0.CO;2.

Kruse, C. G., R. B. Smith, and S. D. Eckermann, 2016: The midlatitude lower-stratospheric mountain wave "valve layer." *J. Atmos. Sci.*, **73**, 5081–5100, https://doi.org/10.1175/JAS-D-16-0173.1.

Le Pichon, A., and Coauthors, 2015: Comparison of co-located independent ground-based middle atmospheric wind and temperature measurements with numerical weather prediction models. *J. Geophys. Res. Atmos.*, **120**, 8318–8331, https://doi.org/10.1002/2015JD023273.

Manney, G. L., and Z. D. Lawrence, 2016: The major stratospheric final warming in 2016: Dispersal of vortex air and termination of Arctic chemical ozone loss. *Atmos. Chem. Phys.*, **16**, 15 371–15 396, https://doi.org/10.5194/acp-16-15371-2016.

Matthias, V., A. Dörnbrack, and G. Stober, 2016: The extraordinarily strong and cold polar vortex in the early northern winter 2015/2016. *Geophys. Res. Lett.*, **43**, 12 287–12 294, https://doi.org/10.1002/2016GL071676.

Mixa, T., A. Dörnbrack, and M. Rapp, 2021: Nonlinear simulations of gravity wave tunneling and breaking over Auckland Island. *J. Atmos. Sci.*, **78**, 1567–1582, https://doi.org/10.1175/JAS-D-20-0230.1.

Morgan, M. C., and J. W. Nielsen-Gammon, 1998: Using tropopause maps to diagnose midlatitude weather systems. *Mon. Wea. Rev.*, **126**, 2555–2579, https://doi.org/10.1175/1520-0493(1998)126<2555:UTMTDM>2.0.CO;2.

Pedlosky, J., 1987: *Geophysical Fluid Dynamics*. 1st ed. Springer-Verlag, 710 pp., https://doi.org/10.1007/978-1-4612-4650-3.

Plougonven, R., and H. Teitelbaum, 2003: Comparison of a large-scale inertia-gravity wave as seen in the ECMWF analyses and from radiosondes. *Geophys. Res. Lett.*, **30**, 1954, https://doi.org/10.1029/2003GL017716.

——, and F. Zhang, 2014: Internal gravity waves from atmospheric jets and fronts. *Rev. Geophys.*, **52**, 33–76, https://doi.org/10.1002/2012RG000419.

Polichtchouk, I., and Coauthors, 2021: Stratospheric modelling and assimilation. ECMWF Tech. Memo. 877, 63 pp., https://doi.org/10.21957/25hegfoq.

Preusse, P., A. Dörnbrack, S. D. Eckermann, M. Riese, B. Schaeler, J. T. Bacmeister, D. Broutman, and K. U. Grossmann, 2002: Space-based measurements of stratospheric mountain waves by CRISTA: 1. Sensitivity, analysis method, and a case study. *J. Geophys. Res.*, **107**, 8178, https://doi.org/10.1029/2001JD000699.

——, M. Ern, P. Bechtold, S. D. Eckermann, S. Kalisch, Q. T. Trinh, and M. Riese, 2014: Characteristics of gravity waves resolved by ECMWF. *Atmos. Chem. Phys.*, **14**, 10 483–10 508, https://doi.org/10.5194/acp-14-10483-2014.

Rapp, M., and Coauthors, 2021: SOUTHTRAC-GW: An airborne field campaign to explore gravity wave dynamics at the world's strongest hotspot. *Bull. Amer. Meteor. Soc.*, **102**, 1–60, https://doi.org/10.1175/BAMS-D-20-0034.1.

Rowe, S. M., and M. H. Hitchman, 2015: On the role of inertial instability in stratosphere–troposphere exchange near mid-latitude cyclones. *J. Atmos. Sci.*, **72**, 2131–2151, https://doi.org/10.1175/JAS-D-14-0210.1.

Sato, K., and M. Yoshiki, 2008: Gravity wave generation around the polar vortex in the stratosphere revealed by 3-hourly radiosonde observations at Syowa Station. *J. Atmos. Sci.*, **65**, 3719–3735, https://doi.org/10.1175/2008JAS2539.1.

——, S. Tateno, S. Watanabe, and Y. Kawatani, 2012: Gravity wave characteristics in the Southern Hemisphere revealed by a high-resolution middle-atmosphere general circulation model. *J. Atmos. Sci.*, **69**, 1378–1396, https://doi.org/10.1175/JAS-D-11-0101.1.

Schoeberl, M. R., 1985: The penetration of mountain waves into the middle atmosphere. *J. Atmos. Sci.*, **42**, 2856–2864, https://doi.org/10.1175/1520-0469(1985)042<2856:TPOMWI>2.0.CO;2.

——, and P. A. Newman, 2015: Middle atmosphere: Polar vortex. *Encyclopedia of Atmospheric Sciences*, G. R. North, J. Pyle, and F. Zhang, Eds., 2nd ed., Academic Press, 12–17, https://doi.org/10.1016/B978-0-12-382225-3.00228-0.

Schumann, U., 2019: The horizontal spectrum of vertical velocities near the tropopause from global to gravity wave scales. *J. Atmos. Sci.*, **76**, 3847–3862, https://doi.org/10.1175/JAS-D-19-0160.1.

Shapiro, M. A., and D. Keyser, 1990: Fronts, jet streams and the tropopause. *Extratropical Cyclones: The Erik Palmén Memorial Volume*, Amer. Meteor. Soc., 167–191, https://doi.org/10.1007/978-1-944970-33-8_10.

Smith, R. B., 1980: Linear theory of stratified hydrostatic flow past an isolated mountain. *Tellus*, **32**, 348–364, https://doi.org/10.3402/tellusa.v32i4.10590.

——, B. K. Woods, J. Jensen, W. A. Cooper, J. D. Doyle, Q. Jiang, and V. Grubišić, 2008: Mountain waves entering the stratosphere. *J. Atmos. Sci.*, **65**, 2543–2562, https://doi.org/10.1175/2007JAS2598.1.

——, and Coauthors, 2016: Stratospheric gravity wave fluxes and scales during DEEPWAVE. *J. Atmos. Sci.*, **73**, 2851–2869, https://doi.org/10.1175/JAS-D-15-0324.1.

Tateno, S., and K. Sato, 2008: A study of inertia-gravity waves in the middle stratosphere based on intensive radiosonde observations. *J. Meteor. Soc. Japan*, **86**, 719–732, https://doi.org/10.2151/jmsj.86.719.

Vallis, G. K., 2017: *Atmospheric and Oceanic Fluid Dynamics: Fundamentals and Large-Scale Circulation*. 2nd ed. Cambridge University Press, 946 pp., https://doi.org/10.1017/9781107588417.

Voigt, C., and Coauthors, 2018: Widespread polar stratospheric ice clouds in the 2015–2016 Arctic winter—Implications for ice nucleation. *Atmos. Chem. Phys.*, **18**, 15 623–15 641, https://doi.org/10.5194/acp-18-15623-2018.

Wagner, J., and Coauthors, 2017: Observed versus simulated mountain waves over Scandinavia—Improvement of vertical winds, energy and momentum fluxes by enhanced model resolution? *Atmos. Chem. Phys.*, **17**, 4031–4052, https://doi.org/10.5194/acp-17-4031-2017.

Wang, S., F. Zhang, and C. Snyder, 2009: Generation and propagation of inertia–gravity waves from vortex dipoles and jets. *J. Atmos. Sci.*, **66**, 1294–1314, https://doi.org/10.1175/2008JAS2830.1.

Woiwode, W., and Coauthors, 2018: Mesoscale fine structure of a tropopause fold over mountains. *Atmos. Chem. Phys.*, **18**, 15 643–15 667, https://doi.org/10.5194/acp-18-15643-2018.

Žagar, N., D. Jelić, M. Blaauw, and P. Bechtold, 2017: Energy spectra and inertia–gravity waves in global analyses. *J. Atmos. Sci.*, **74**, 2447–2466, https://doi.org/10.1175/JAS-D-16-0341.1.

Zhang, F., S. E. Koch, C. A. Davis, and M. L. Kaplan, 2000: A survey of unbalanced flow diagnostics and their application. *Adv. Atmos. Sci.*, **17**, 165–183, https://doi.org/10.1007/s00376-000-0001-1.

——, C. A. Davis, M. L. Kaplan, and S. E. Koch, 2001: Wavelet analysis and the governing dynamics of a large-amplitude mesoscale gravity-wave event along the East Coast of the United States. *Quart. J. Roy. Meteor. Soc.*, **127**, 2209–2245, https://doi.org/10.1002/qj.49712757702.